

Numerical modelling of the growth of polygonal fault systems

James J. King^{a,*}, Daniel T. Roberts^b, Joe A. Cartwright^a, Bruce K. Levell^a

^a Department of Earth Sciences, University of Oxford, Oxford, OX1 3AN, UK

^b Rockfield Software Ltd., Swansea, SA1 8AS, UK

ARTICLE INFO

Keywords:

Polygonal fault systems
Differential compaction
Numerical modelling
Fault displacement
Fault growth
Fine-grained sediment dewatering
Soil mechanics

ABSTRACT

Despite over three-decades of active research and wide debate in the published literature, the mechanisms that govern the growth of polygonal faults are poorly understood. Here we investigate the growth of polygonal faults using a suite of geomechanical finite element forward models that couple dynamic fault propagation, sedimentation, and the mechanical compaction of unconsolidated granular sediment. We undertook a suite of numerical model simulations to explore the relationships between varying fault plane dip, residual friction of the fault, and the bulk material properties of the sedimentary sequence hosting the polygonal fault system. We find that the growth of polygonal faults within laterally-pinned sedimentary tiers can be explained by gravity-driven differential compaction and does not require additional causative elements to explain the gross pattern of strain accumulation. We also find that the magnitude of fault throw is influenced by the material properties and the original fault plane dip, but is most sensitive to the residual friction angle. Our models yield values for maximum throw versus height for the faults that fall within the range of global values compiled for polygonal faults, and throw rates are comparable to those recently measured in naturally occurring polygonal faults.

1. Introduction

Polygonal fault systems (PFSs) were first recognised as a form of intra-formational or 'layer-bound' faulting in the late 1980's (Henriet et al., 1988; Higgs and McClay, 1993) and were subsequently linked with the diagnostic polygonal planform with the advent of three-dimensional seismic mapping in the 1990s (Cartwright, 1994; Lonergan et al., 1998a,b). They have subsequently been documented in over 150 basins around the world, where they typically span areas of 10^5 – 10^7 km² and occur in stratigraphically restricted intervals (tiers) composed dominantly of fine-grained sediments (Fig. 1) (Cartwright, 2011 and references therein).

The widespread occurrence of PFSs within the shallow subsurface of many slope or basin floor settings suggests they initiate and begin to propagate early in the burial history of the host tier (Cartwright, 1994a,b; Berndt et al., 2003; Stuevold et al., 2003), perhaps within tens of metres of the sea floor (Morgan et al., 2015). Numerous studies have suggested that polygonal faults propagate upwards through the near surface sediments with continued burial and sedimentation (Lonergan et al., 1998a; Goult, 2001a; Stuevold et al., 2003; Gay and Berndt, 2007; Davies and Ireland, 2011; Tewksbury et al., 2014). The important question of whether or not polygonal faults can be regarded as

syn-sedimentary faults in which the upper fault tip breaches the contemporaneous depositional surface is still open, although several authors have used growth indices or fault network characteristics to argue that this is generally the case (Lonergan et al., 1998a; Stuevold et al., 2003; Morgan et al., 2015). Most recently, King and Cartwright (2020) identified small bathymetric scarps on the present sea floor offshore Norway to argue that these were the surface expression of syn-sedimentary polygonal faults, confirming similar observations made in the Rockall Trough by Berndt et al. (2012).

Several mechanisms have been proposed to explain the nucleation and growth of PFSs, but most have been discounted as universal mechanisms because they cannot explain the formation or growth of all polygonal fault systems observed globally (Cartwright et al., 2003; Goult, 2008; Cartwright, 2011). In recent years, 'gravitational loading' (Goult, 2001a; Goult and Swarbrick, 2005) and 'diagenetically-induced shear failure' (Shin et al., 2008, 2010; Cartwright, 2011) have been favoured as mechanisms to explain the later propagation and early initiation of polygonal faults, respectively.

The gravitational loading mechanism is the main focus of our modelling study presented in this paper. It provides an elegant geomechanical explanation of the upward propagation of already well developed fault zones with increasing sediment loads of progressive

* Corresponding author.

E-mail address: jamesking100@btinternet.com (J.J. King).

<https://doi.org/10.1016/j.jsg.2022.104679>

Received 2 January 2022; Received in revised form 2 July 2022; Accepted 7 July 2022

Available online 16 July 2022

0191-8141/© 2022 The Authors. Published by Elsevier Ltd. This is an open access article under the CC BY license (<http://creativecommons.org/licenses/by/4.0/>).

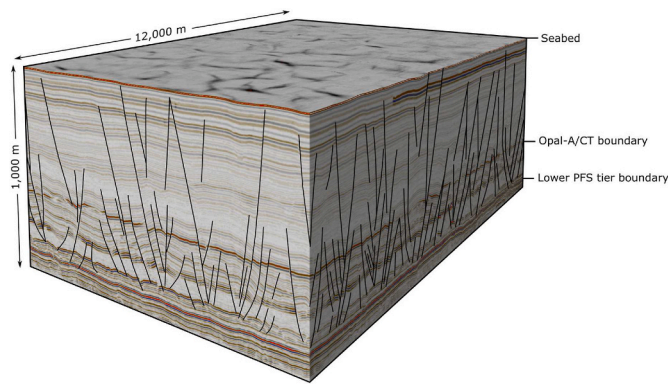


Fig. 1. A three-dimensional visualisation of a portion of the Vøring Basin PFS, Norwegian Sea, showing the geometry of polygonal faults in cross-section and the classic polygonal planform pattern at the present-day seabed.

burial (Goult, 2001a,b; Goult and Swarbrick, 2005; Goult, 2008). The residual failure criterion of a pre-existing fault is exceeded under laterally confined loading conditions (Fig. 2 A) if it is hosted within a material with a sufficiently low residual friction angle and a high K_0 value. K_0 is the coefficient of lateral earth pressure 'at rest', calculated as the ratio of the horizontal effective stress over the vertical effective stress, which is typically ~ 0.3 – 0.4 for coarse-grained sediments and >0.7 for fine-grained sediments (Jones, 1994; Goult, 2001a; Goult and Swarbrick, 2005; Casey, 2014). However, the gravitational loading mechanism does not explain either the nucleation of polygonal faults or how displacement is accommodated.

In contrast, it has been suggested that the diagenetically-induced shear failure mechanism may explain the full evolution of a PFS, from genesis to fossilisation (Shin et al., 2008, 2010; Cartwright, 2011). In

this model, a diagenetically-induced change in the grain volume or contact stresses between grains results in a decrease in the minimum principal stress, which can cause the localisation and continued propagation of a shear fracture. Furthermore, the volumetric reduction associated with such a diagenetic mechanism can help accommodate the local strains required by displacement gradients on the fault surface in laterally-pinned conditions (Shin et al., 2008).

Attempts at resolving the relative merits of competing models using numerical modelling have been limited to date. Shin et al. (2010) used a Drucker-Prager model to investigate the physical properties that are required to accommodate the strain and deformation that arise from the growth of a laterally-pinned fault. Shin et al. (2010) found that the throw-to-height scaling relationships of polygonal faults were only achieved at exceptionally low material bulk stiffness values and attributed this finding to diagenetic grain dissolution, following results from earlier physical modelling work (Shin et al., 2008). However, the bulk material stiffness term used in the Shin et al. (2010) Drucker-Prager models does not explicitly incorporate gravity-driven mechanical compaction of granular sediment. Roberts et al. (2014) and Roberts (2014) used the ELFEN geomechanical code and a *SoftRock 3* constitutive model to demonstrate that a diagenetically-triggered isotropic chemical porosity reduction, such as that caused by the transition of opal-A to opal-CT, of 5% was sufficient to localise and propagate shear fractures that resembled the geometries and network intersections of polygonal faults in two-dimensional cross-section and three-dimensional planforms. Roberts et al. (2014) and Roberts (2014) also showed that a horizontal stress anisotropy of just 3% was enough to align over 80% of fault orientations to within $\pm 10^\circ$ of the maximum horizontal stress. Despite the advances made by these pioneering studies, our understanding of the relative magnitudes of different drivers of PFS growth is limited, and the role of gravity-driven mechanical compaction may have been overlooked as a means of accommodating polygonal fault displacement.

In this study, we used the gravitational loading model proposed by Goult (2001) as a basis to numerically model the hypothesis that gravity-driven differential compaction drives the accumulation of throw on pre-existing polygonal faults that are hosted in laterally-pinned (i.e. the lateral boundaries of the model are fixed) unconsolidated sediments, under realistic physical property conditions. To test the model, we developed a series of laterally-pinned finite element models using the ELFEN geomechanical code, to examine the evolution of a single fault that propagates synchronously with the deposition of granular compacting sediment. We investigated the sensitivity of the accrual of fault displacement with respect to three main variables: (1) material compaction profiles, (2) residual friction angles, and (3) fault dip angles, in order to evaluate under what conditions the continued propagation of a normal fault might be driven by gravitational loading alone. Although aimed at the study of polygonal fault systematics, this type of modelling approach is applicable to other types of normal faults hosted in relatively un lithified and compactable sediments, so the results have wider implications than simply for PFSs.

2. Methodology

2.1. Computational framework

To undertake our analysis, we used the ELFEN forward modelling geomechanical code, which is a finite strain, quasi-static, explicit finite element continuum formulation. The underlying computational methods are discussed extensively by Perić and Crook (2004). This modelling framework has been used to solve a host of geological problems ranging from salt tectonics (Nikolinakou et al., 2014a,b) to regional fold and thrust belts (Albertz and Lingrey, 2012), as well as previous studies of polygonal fault systems (Roberts et al., 2014; Roberts, 2014). However, alternative modelling approaches such as the Discrete Element Method (DEM), which unlike the finite element continuum

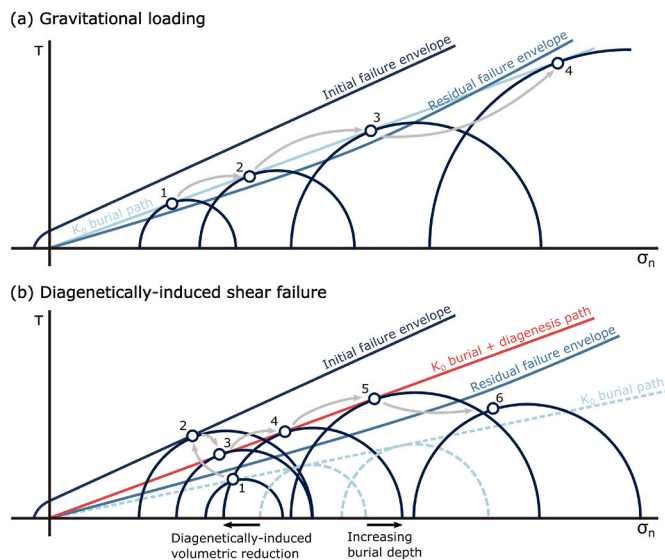


Fig. 2. Illustrative representation of the (a) gravitational loading mechanism and (b) diagenetically-induced shear failure mechanism presented in terms of Mohr-Coulomb theory, with effective normal stress acting on the shear plane (σ_n) on the x-axis and shear stress (τ) on the y-axis. The gravitational loading mechanism may explain the propagation of pre-existing fractures that are hosted within laterally-pinned materials with low intrinsic residual friction angles and high K_0 values. Diagenetic changes in the physical properties of laterally-pinned sediments may cause a reduction in the minimum principal stress such that the size of the Mohr circle increases to intersect the initial failure envelope, thus causing the nucleation of a shear fracture. Continued diagenesis with increasing burial may yield conditions that exceed the residual failure envelope until the cessation or slowing of diagenetic activity.

approach does not use a pre-defined material constitutive model but instead models the interaction of rock particle assemblages governed by Newton's laws of motion, have been used to solve similar geological problems (Finch et al., 2003; Schöpfer et al., 2009; Gray et al., 2014). We selected a finite element approach because the DEM approach can require excessively long solution times due to the searches needed to evaluate the particle interactions, which can therefore limit the model resolution (Yinet al., 2009), and the calibration of some DEM models can present challenges in obtaining values recorded from physical experiments (Schöpfer et al., 2009). The ability to pre-define the material behaviour in a continuum approach offered greater specificity when designing a sensitivity analysis of granular material compaction trends, and previous studies of PFSs using these modelling tools provided a proof of concept prior to embarking on our study. However, both the finite element and discrete element methods offer valid approaches to the study of polygonal fault systems.

2.2. Constitutive model

The constitutive model relates deformational strains and stresses through a set of equations (see *Supplementary Material* for detailed descriptions) that comprise material-specific parameters, such as frictional and dilational angles. We used the *SoftRock 3* (SR3) constitutive model, which is an advanced variant of the Modified Cam Clay model (Crook et al., 2006) that is derived from Critical State Soil Mechanics theory (Schofield and Wroth, 1968; Muir Wood, 1990), in our study because it explicitly incorporates the role of granular sediment compaction in material deformation. Alternative constitutive frameworks, such as the Mohr-Coulomb and Drucker-Prager models have been used in several computational geological studies (Schultz-Ela, 2003; Gradmann et al., 2009; Shin et al., 2010), however, they do not explicitly account for granular compaction and are therefore, better suited to the characterisation of lithified and crystalline rocks. Several previous studies have used an SR3 constitutive framework to model the elastoplastic deformation associated with salt diapirs rising through porous sediments (Nikolinakou et al., 2014a,b), and the investigation of polygonal faulting in unconsolidated fine-grained sediments (Roberts et al., 2014; Roberts, 2014).

The methodology and calibration of the *SoftRock 3* constitutive framework are discussed extensively by Crook et al. (2006), Rockfield (2010), and Roberts et al. (2014). This approach offers a fully regularised treatment of softening and identification of emerging localisations, extending the seminal work of Rudnicki and Rice (1975). The full elastoplastic formulation is included in the *Supplementary Material*, however, we use a reduced subset of its full capability in our analysis. Specifically, rather than determining the nucleation and propagation of the fault plane via the intersection of the material stress path with the

state boundary surface as in the diagenetically-induced fault nucleation simulations undertaken by Roberts et al. (2014), we instead prescribe the fault with a frictional planar surface. In addition, the *SoftRock 3* constitutive framework includes a porous elastic law that is included in our simulations, but its influence is negligible over the burial depths of our material models which are instead primarily deforming via compaction-related plastic strain determined by the hardening law (see *Supplementary Material*).

2.3. Model setup

2.3.1. Modelling strategy

Our modelling strategy was designed to test the gravitational loading model for polygonal fault growth. Our primary goal was to investigate the extent to which stress perturbations related to low friction coefficients on a fully developed fault surface would result in differential compaction of hanging wall versus footwall (Fig. 3). We constructed a suite of two-dimensional field-scale finite element models that simulate the upward propagation of a pre-existing normal fault from a fixed lower tip with synchronous sedimentation in laterally-pinned plane-strain conditions. We assumed that the pore fluid pressure was hydrostatic throughout the evolution of the model simulations, based on the recognition that polygonal fault systems are commonly hosted in hemipelagic depositional systems with low sedimentation rates in which significant disequilibrium compaction overpressure is unlikely to develop (Cartwright and Dewhurst, 1998 and references therein).

The numerical modelling programme was designed to allow a sensitivity analysis of the accrual of fault throw with respect to three key variable parameters. Firstly, the bulk lithology of the sequence hosting a polygonal fault and its typical compactional response to burial. Since polygonal fault systems are hosted in a range of dominantly fine-grained lithologies, it was regarded as important to capture the compactional response of this broad range of materials. Secondly, the friction angle of the fault plane (residual friction angle), because as argued by Goult (2002), this should be a critical parameter governing conditions allowing continued slip on the fault. Finally, the dip angle at which the fault plane propagates since this partly controls the shear stress resolved on the fault plane.

The models comprise a thin initially deposited basal unit that hosts a pre-existing fault plane which then propagates upwards from a fixed lower tip within that basal unit as additional layers are added above (Fig. 3). The upward fault propagation occurs synchronously with the deposition of 1000 m of unconsolidated granular material at a sedimentation rate of 100 m/m.y. over fifty 0.2 million-year time increments, simulating 10 million-years. Downward propagation of the basal tip is inhibited by detachment at the lower boundary of the model (see next section).

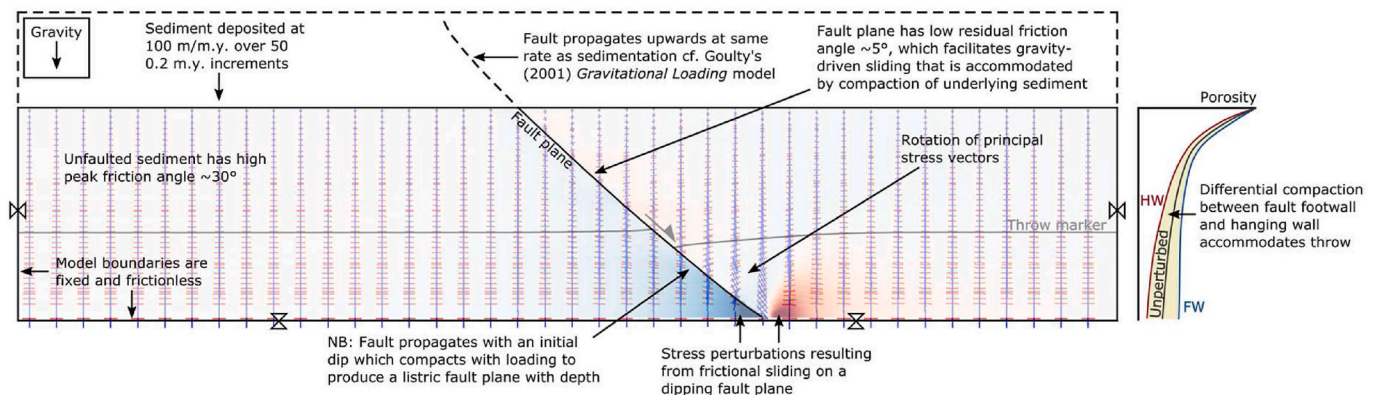


Fig. 3. Schematic illustration of model set-up. Base colours represent effective mean stress. (For interpretation of the references to colour in this figure legend, the reader is referred to the Web version of this article.)

Material compaction is fully coupled throughout all fifty depositional stages, where we assume fully-drained conditions with no build-up of overpressure. The material compaction profile, the initial fault plane dip and residual friction angle are prescribed for each model simulation, and their respective influences on fault throw are investigated via sensitivity analysis. The material compaction profile with increasing burial depth is prescribed in each simulation, where we investigate four primary compaction curves (outlined in [Section 3.3.3](#)). The fault plane friction angle (residual friction angle) remains constant in each simulation, and is investigated over values of 5°, 7°, 9°, and 11°. The fault dip angle is prescribed on the upper tip segment that propagates at each 0.2 million-year time increment, however, the fault dip angle shallows dynamically with burial as a result of compaction creating a degree of fault dip listricity. We investigate initial dip angle values of 40°, 50°, 60°, 70°, and 80°, which when compacted shallow by as much as 15°–20° at depth. These values were selected from the range of natural dip measurements of polygonal faults ([Neagu et al., 2010](#)).

2.3.2. Boundary conditions

The width of the models are set so that there is no interaction between fault-related deformations in the central portion of the model and the lateral boundary conditions, and vice versa. All models are 2000 m wide with element sizes of ~5 m, except for the investigation of a 40° dipping fault plane which requires a 3000 m wide model to prevent edge effects. All of the models have frictionless boundary conditions at both their lateral edges and base, where elements at the model boundaries are confined but are able to slide freely. The basal slip condition was selected to represent natural examples where a basal detachment has been interpreted at the base of regional polygonally faulted tiers ([Cartwright, 2011](#)) and may also be considered akin to an overpressured basal mobile layer as suggested by [Nicol et al. \(2003\)](#). We note that a fully-fixed basal boundary condition also produces appreciable displacement.

2.3.3. Material characterisation

We characterised four materials, m1–m4, to capture a range of different compaction profiles that are exhibited by fine-grained sediments. All materials used in our analysis are characterised with the same

underlying elastic physical property and SR3 property parameters (see *Supplementary Material*, Tables SM1 and SM2), however, each material has a unique compaction profile that is defined by a piecewise linear lambda-kappa parameter in the hardening law (see *Supplementary Material*) all with an initial porosity value of 70%.

Over the shallow burial depths analysed in our models, gravitationally-driven volumetric strains of high porosity granular sediments are predominately plastic rather than elastic. We include the SR3 porous elastic laws (see *Supplementary Material*) in our material characterisation for completeness, however, our models are insensitive to changes in both the stiffness parameter value (E) and Poisson's ratio parameter value (ν) that fall within the range of those recorded from fine-grained sediments ([Santamarina et al., 2001](#)). Furthermore, the SR3 property parameters used to define the state boundary surface are included (see *Supplementary Material*). It should be noted that fault plane propagation is prescribed in our models rather than determined via the intersection of the material stress path with the state boundary surface. The SR3 frictional and dilational parameters were chosen such that the material is characterised with a K_0 value of 0.7–0.72 typical of fine-grained sediments ([Jones, 1994](#); [Goult and Swarbrick, 2005](#); [Casey, 2014](#)).

The compaction profiles that define each material (m1–m4) have been guided by consideration of compaction curves from shales and argillaceous sediments, experimental compaction curves derived from kaolinite-smectite aggregates, and porosity-versus-depth data from Ocean Drilling Program (ODP) wells that logged four different polygonal fault systems ([Fig. 4](#)). These reference compaction curves were selected to capture the range of natural compaction behaviour in the shallow burial regime typical of the growth of polygonal fault systems ([Cartwright et al., 2003](#)). They define the trajectory of a given starting lithology in porosity-depth space, yielding incremental differences in both the gradient of compaction with depth and the absolute amount of compaction. The m1, m2, and m3 materials are defined to capture the upper, middle, and lower ranges of compaction curve profiles recorded from fine-grained sediments in previous compaction studies (compiled in [Mondol et al., 2007](#)). The m4 material more closely traces the porosity versus depth profiles of biosiliceous fine-grained sediments recorded from ODP boreholes that transect known polygonal fault systems

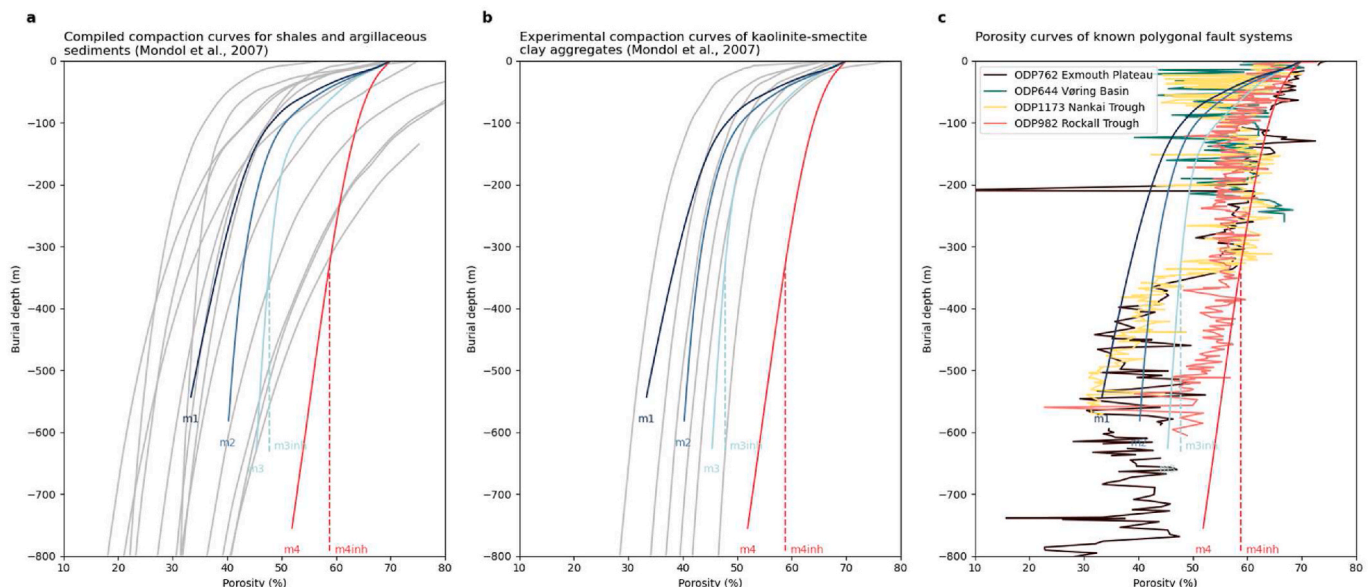


Fig. 4. Compaction curves for the m1, m2, m3, m4, m3inh, and m4inh materials used in our sensitivity study superimposed on: (a) Compaction curves for shales and argillaceous sediments from several literature sources compiled in [Mondol et al. \(2007\)](#); (b) Experimental compaction curves of kaolinite-smectite clay aggregates from [Mondol et al. \(2007\)](#). Ratios of kaolinite:smectite aggregates of grey coloured compaction curves from left to right 100:0, 80:20, 60:40, 40:60, 20:80, 0:100.; (c) Porosity versus depth curves from Ocean Drilling Program (ODP) well sites that transect known polygonal fault systems that are hosted in fine-grained sediments ranging in lithology from claystone (upper ~300 m of Vøring Basin PFS), siliceous mudstone (Nankai Trough PFS), to calcareous ooze (Exmouth Plateau PFS).

(Shipboard Scientific Party, 1987,1990, 1996, 2001). After the first 150 m of burial the compaction gradients of the m1 and m4 materials are approximately equal, which presents an opportunity to compare the influence of the absolute magnitude and the gradient of volumetric reduction on the accrual of fault throw.

The material residual friction angle (fault friction angle) is a variable parameter that is investigated through sensitivity analysis over values between 5° and 11°. This range of values was selected based on experimental data from ring shear, drained shear box, and rotary shear tests of claystones and siliceous mudstones (Table 1). It is challenging to scale up from experimental measurements of residual shear strength to the effective residual shear strength of a natural fault zone many tens to hundreds of metres tall and perhaps tens of centimetres wide. However, in the absence of any data from natural faults the experimentally derived values were considered to be the best starting point for this modelling study.

2.3.4. Model outputs

A standard set of outputs was generated for each model simulation, including effective mean stress, effective mean stress perturbation, horizontal effective mean stress perturbation, vertical effective mean stress perturbation, and vector plots of principal stress values. Fault throw was measured as the throw at each stratigraphic marker along the fault plane for each growth increment. Throw was measured rather than displacement to enable ease of comparison to previous polygonal fault studies, in which throw is the standard measure derived from seismic reflection datasets. These measurements were plotted as throw versus height profiles. Maximum throw (T_{\max}) against fault height ratios were generated for the full suite of model simulations and were benchmarked to the global range of T_{\max} versus height values compiled by Shin et al. (2010). Throw rates for the final stages of each model simulation were derived by taking the throw value at the stratigraphic marker deposited one million years before the present timestep.

2.3.5. Kinematic justification

The kinematics of our fault propagation models are based on previous studies that have shown: (1) polygonal faults nucleate in the lower portions of their tiers early in their burial history (Cartwright et al., 2003); (2) polygonal faults propagate in an upwards direction for much of their growth histories (Morgan et al., 2015), where their downward propagation is impeded by a basal mechanical barrier or a detachment into a mobile basal layer (Cartwright et al., 2003; Cartwright, 2011); (3) polygonal fault systems are found at the present day (Gay and Berndt,

2007; Berndt et al., 2012; Armandita et al., 2015; Morgan et al., 2015) and paleo-seabed, as evidenced by small growth packages (Cartwright, 1994a, 2011; Lonergan et al., 1998a; Stuevold et al., 2003; Laurent et al., 2012; King and Cartwright, 2020), which suggests that polygonal faults can propagate upwards at or near the seabed; (4) fault propagation may occur synchronously with gravitational loading in sediments with sufficiently high K_0 values and sufficiently low residual friction angles (Goult, 2001a; Goult and Swarbrick, 2005) (Fig. 2 A); (5) hemipelagic sedimentation rates in deep marine depositional environments are low (~2–200 m/m.y.) (Cartwright and Dewhurst, 1998; Shipboard Scientific Party, 1987, 1990, 1996, 2001).

Geometrical and quantitative measures to compare our modelling results and test our hypothesis are offered by the maximum throw (T_{\max}) versus height empirical scaling relationship established by Shin et al. (2010), and a plethora of polygonal fault throw versus height profiles from multiple basins around the world (Neagu et al., 2010; Turrini et al., 2017; Wrona et al., 2017). Recently recorded throw rates from surface-breaching polygonal fault upper tips from the Vøring Basin (King and Cartwright, 2020) were used to compare with growth rates generated in the models.

3. Results

In order to obtain adequate comparisons of model outputs for the three main variable parameters of friction, dip, and material compaction properties (Fig. 5), outputs were generated for a total of 18 numerical model simulations. An illustrative example of the temporal evolution of a single fault growth model is shown in Figs. 6 and 7 for the m1-fr5-d60 model (where m1 is the material model, fr5 represents the residual friction angle used was 5°, and d60 represents the fault propagated with a dip angle of 60°) at 2 million-year time increments. A principal stress vector plot for this model at the 10 million-year timestep is presented in Fig. 8. This shows that there is considerable rotation of the maximum and minimum stresses associated with frictional sliding on the fault plane (Mandl, 1988). The stress field is unperturbed at the lateral edges of the models, where the effective mean stress increases monotonically with depth as the result of one-dimensional consolidation (Terzaghi and Peck, 1948). Effective mean stress perturbations are found on both sides of the fault plane, where they dissipate to ambient values within a few hundred metres of the fault plane (Fig. 6). The results of our full suite of model simulations are illustrated in Fig. 5.

Table 1

Low residual friction angle values recorded from fine-grained sediments compiled from published literature.

Residual friction angle (°)	Lithology	Age	Location	Method	References
3.4	Wet montmorillonite	–	–	Drained triaxial friction experiments	Moore and Lockner (2007)
4.6	Claystone – Santa Clara Fm	Plio-Pleistocene	Santa Clara California, USA	Drained shear box	Nelson (1992)
4.9	Siliceous mudstone - Honorable	–	Honorable URL site, Japan	–	Sanada et al. (2009)
5.0	Claystone	–	Chatfield Dam, Colorado, USA	Drained ring shear	Dewoolkar and Huzjak (2005)
5.0	Claystone	Plio-Pleistocene	Oahu, Hawaii	Drained ring shear	Wan and Kwong (2002)
5.1	Claystone	Lower Miocene	North Sea	Leak-off test estimate	Goult and Swarbrick (2005)
5.7	Claystone – Cucaracha Clay	Early-Middle Miocene	Panama Canal	Drained ring shear and drained shear box	La Gatta (1970) and Bishop et al. (1971)
6.0	Claystone – Weald Clay	Cretaceous	Kent, UK	Drained shear box	Cripps and Taylor (1981)
6.2	Claystone – Nankai Trough	–	Nankai Trough, offshore Japan	Rotary shear	Ikari et al. (2018)
6.8	Claystone	Late Pleistocene	IODP Hole U1381, offshore Costa Rica	Rotary shear	Namiki et al. (2014)
8.0	Claystone – Blue London Clay	Early Eocene	Wraysbury, UK	Drained ring shear	La Gatta (1970) and Bishop et al. (1971)
8.0	Claystone – Brown London Clay	Early Eocene	Walthamstow, UK	Drained ring shear	Bishop et al. (1971)
10.3	Claystone	Pliocene-Quaternary	Eastern Mediterranean ODP Leg 160	Drained shear box	Kopf et al. (1998)

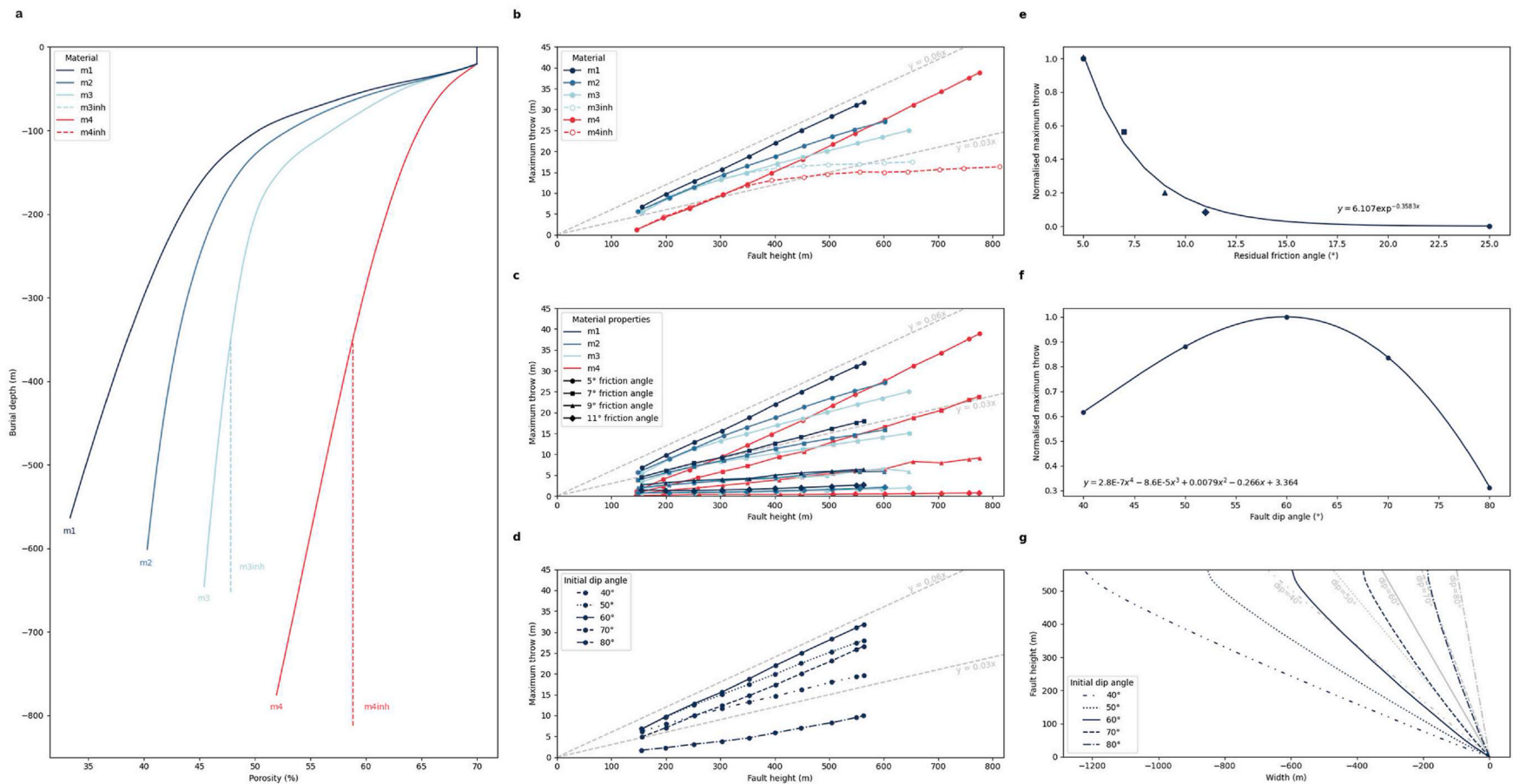


Fig. 5. (a) Solid coloured lines display the compaction profiles of 1000 m of deposited sediment for the four materials, m1-m4, which are derived from published compaction curves for hemipelagic fine-grained sediments. Dashed lines represent inhibited compaction profiles beyond a burial depth of 350 m for the m3inh and m4inh materials. (b) Sensitivity of maximum throw with respect to fault height for a range of compacting and incompressible materials for a fault plane with a propagating dip angle of 60° and a 5° residual friction angle. (c) Sensitivity of maximum throw on a fault plane with a propagating dip angle of 60° with respect to fault height for materials m1-m4 over residual friction angles of 5°, 7°, 9°, and 11°. (d) Sensitivity of maximum throw with respect to fault height for a fault with propagating dip angles between 40° and 80° hosted in the m1 material with a 5° residual friction. (e) Normalised maximum throw values with respect to different residual friction angles on a fault with a propagating dip angle of 60° hosted in the m1 material with a peak friction angle of 25°. (f) Normalised maximum throw values with respect to different initial fault dip angles for a fault with a residual friction angle of 5° hosted in the m1 material. (g) Blue coloured lines show compacted fault dip angles used in our sensitivity analysis for the m1 material at true scale. Grey lines show the initial uncompacted dip angles for visual comparison. (For interpretation of the references to colour in this figure legend, the reader is referred to the Web version of this article.)

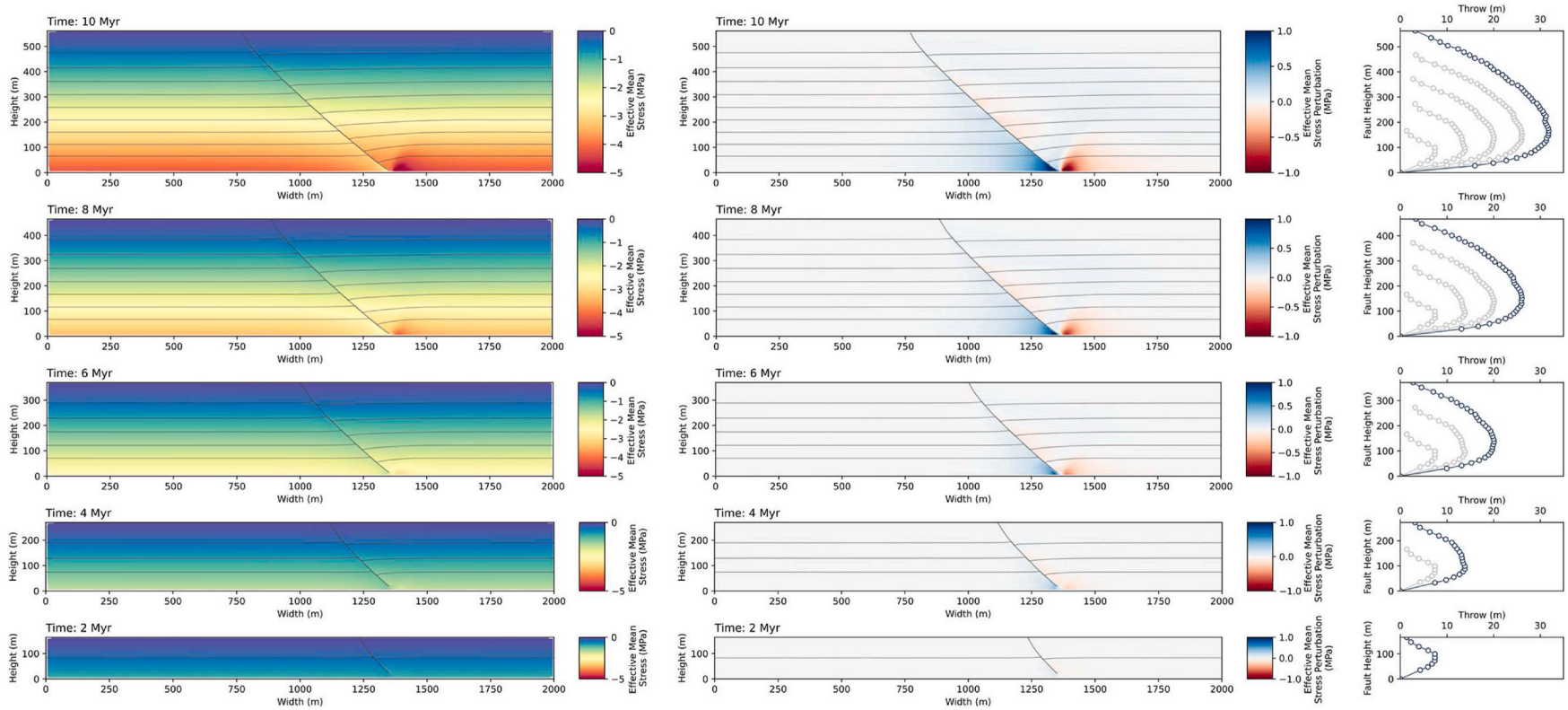


Fig. 6. Effective mean stress and effective mean stress perturbation contour plots at 2 million-year time increments showing the evolution of a normal fault hosted in laterally-pinned conditions that propagates simultaneously with the deposition of granular sediment at a rate of 100 m per million years. The fault propagates with an initial dip of 60° that shallows to $\sim 40^\circ$ with compaction. The residual friction angle is 5° and the host material is characterised by the m1 material compaction profile. Offset grey horizontal lines represent stratigraphic markers at 1 million-year time intervals. The throw versus height graphs that accompany the contour plots display the accrual of vertical displacement throughout the growth of this fault. Points represent throw measurements taken at stratigraphic markers with a 0.2 million-year depositional interval. Blue colours represent the throw profile for the timesteps in the adjacent contour plots and grey coloured profiles represent throw versus height profiles at previous time steps to illustrate the evolution of fault growth. (For interpretation of the references to colour in this figure legend, the reader is referred to the Web version of this article.)

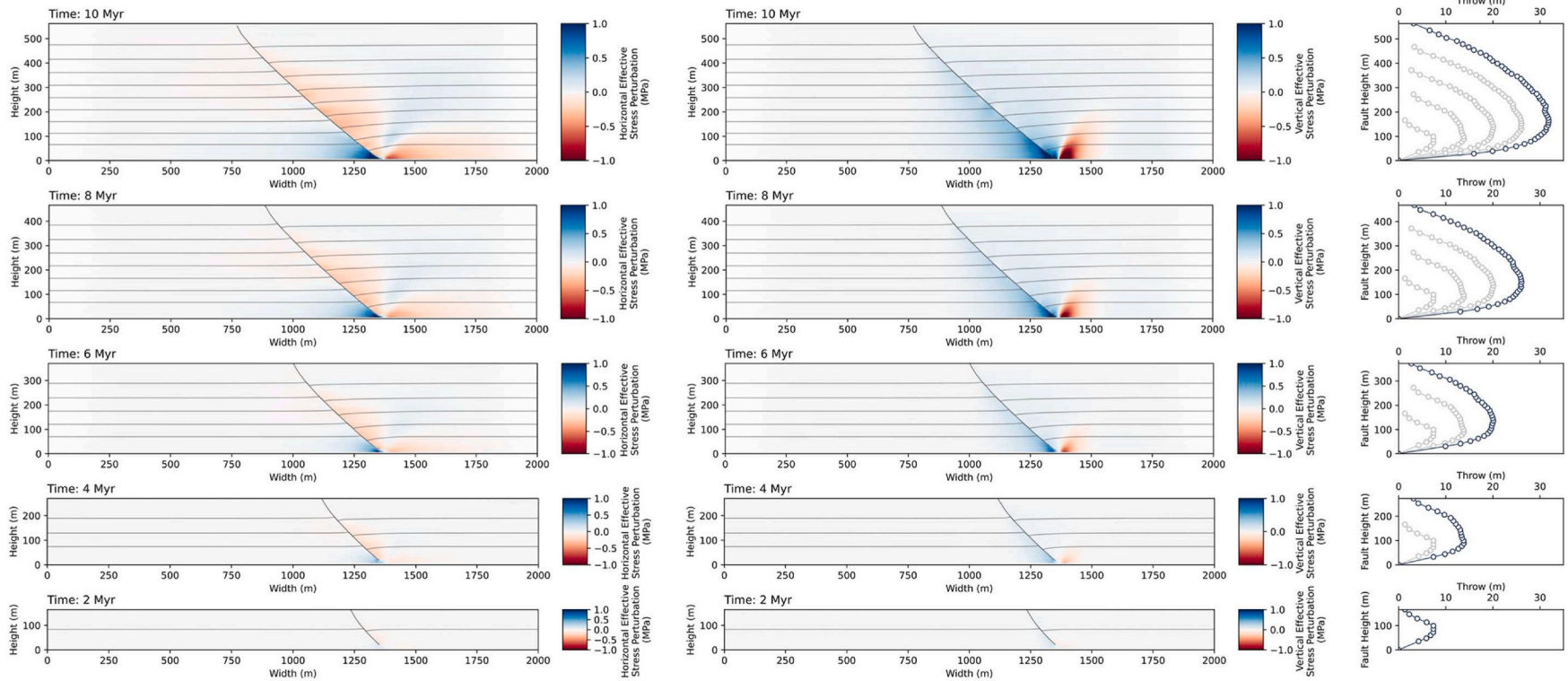


Fig. 7. Horizontal and vertical effective mean stress perturbation contour plots at 2 million-year time increments showing the evolution of a normal fault hosted in laterally-pinned conditions that propagates simultaneously with the deposition of granular sediment at a rate of 100 m per million years. The fault propagates with an initial dip of 60° that shallows to $\sim 40^\circ$ with compaction. The residual friction angle is 5° and the host material is characterised by the m1 material compaction profile. Offset grey horizontal lines represent stratigraphic markers at 1 million-year time intervals. The throw versus height graphs that accompany the contour plots display the accrual of vertical displacement throughout the growth of this fault. Points represent throw measurements taken at stratigraphic markers with a 0.2 million-year depositional interval. Blue colours represent the throw profile for the timesteps in the adjacent contour plots and grey coloured profiles represent throw versus height profiles at previous timesteps to illustrate the evolution of fault growth. (For interpretation of the references to colour in this figure legend, the reader is referred to the Web version of this article.)

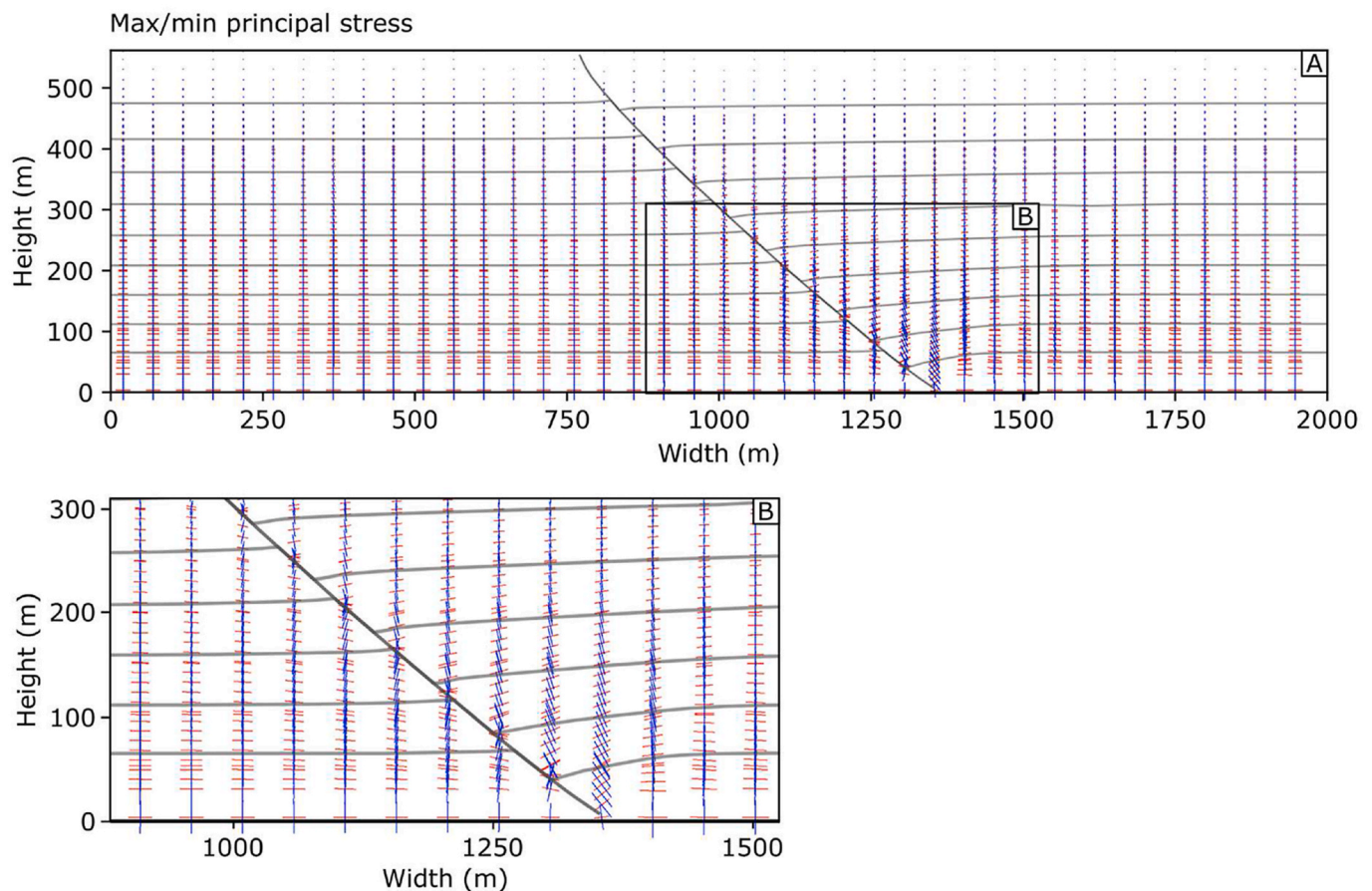


Fig. 8. (A) Maximum (blue) and minimum (red) principal stress vectors at a 50 m spacing for the m1-fr5-d60 model simulation at the final 10 million-year timestep. (B) Shows a zoomed in region centred on the lower fault tip exhibiting rotation of the principal stress axes. The size of the vector symbol scales with the magnitude of the stress, which increases with burial depth. (For interpretation of the references to colour in this figure legend, the reader is referred to the Web version of this article.)

3.1. Material compaction and fault throw

Faults hosted within each of the m1-m4 materials (Fig. 5 A) yield different maximum throw values with respect to the fault height (Fig. 5 B), implying that the compactional response plays a key role in the accumulation of throw. The greatest maximum throw values accrue on faults hosted in the m1 material (Fig. 5 B), which exhibits the largest degree of compaction with burial depth of the four selected material characterisations (Fig. 5 A). Faults hosted in the m2 and m3 materials accrue lower maximum throw values compared to faults hosted in the m1 material (Fig. 5 B), which reflects the incrementally lower compactional strain accumulated with burial depth (Fig. 5 A). Interestingly, faults hosted in the m4 material initially accrue lower maximum throw values than faults hosted in the m2 and m3 materials at heights less than 450 m and 600 m, respectively. However, at fault heights greater than 450 m and 600 m, respectively, the maximum throw values are larger for faults hosted in the m4 material than their m2 and m3 counterparts (Fig. 5 B). The gradient of the T_{\max} versus fault height trends (Fig. 5 B) for faults hosted in the m1 and m4 materials are approximately equal, which reflects the similarities in their compaction profile gradients at burial depths deeper than 150 m (Fig. 5 A). However, faults hosted in the m1 material yield larger maximum throw values than those of faults hosted in our m4 material because of the differences in their compaction profiles in the first 150 m of burial below the surface.

The gradients of the T_{\max} versus fault height trends (Fig. 5 B) for faults hosted in the m2 and m3 materials decrease with increasing fault height in a curvilinear fashion as the rate of material compaction reduces with greater burial depth. In contrast, the near-constant gradients

of the T_{\max} versus fault height trends of faults hosted in the m1 and m4 materials reflect their respective near-constant compaction profiles with burial depths in excess of 150 m (Fig. 5 A). Once the sediment hosting the fault ceases to undergo further compaction, as characterised by the m3inh and m4inh materials (Fig. 5 A) at burial depths greater than ~350 m, the T_{\max} versus fault height gradient decreases dramatically to near-zero with increasing fault height (Fig. 5 B).

The influence of inhibited material compaction with burial depth on the accrual of fault throw is seen most clearly in the effective stress contour plots and accompanying throw versus height plots illustrated in Figs. 9–11. Here we see that throw continues to accumulate in the upper portions of the faults that are hosted in compacting stratigraphy at burial depths shallower than ~350 m, but fault throw ceases to accumulate on deeper portions of the faults that are hosted in stratigraphic intervals which do not undergo compaction (Figs. 9 and 10).

The throw versus height plots of the m3inh and m4inh simulations exhibit flat gradients across the central portion of the fault, where throw values are roughly constant – characteristic of ‘M-style’ faults – and the locus of maximum throw migrates up the fault. This pattern contrasts with that seen for the simulations using material m3 and m4 uninhibited which have T_{\max} values located in the lower to central third of the fault height and ‘C-shaped’ throw versus height profiles (Fig. 11) (Muraoka and Kamata, 1983). The m3inh and m4inh simulations also exhibit elevated effective mean stress perturbations in the lower portion of the tier compared to their m3 and m4 simulations (Figs. 9 and 10).

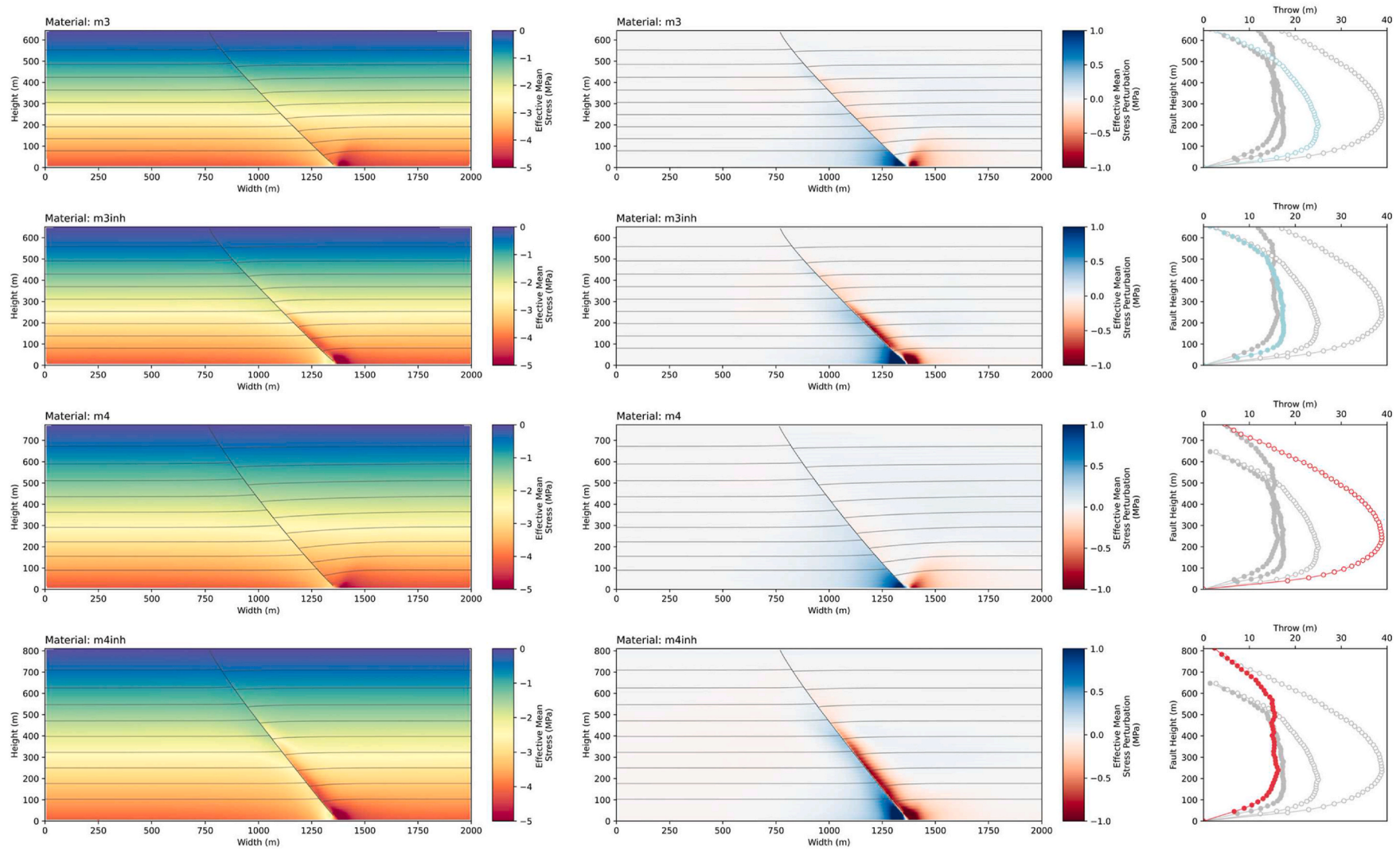


Fig. 9. Effective mean stress and perturbation contour plots and accompanying throw versus height plots for faults with a propagating dip angle of 60° and a residual friction angle of 5° hosted in the m3, m3inh, m4, and m4inh materials at the conclusion of their respective 10 million-year simulations.

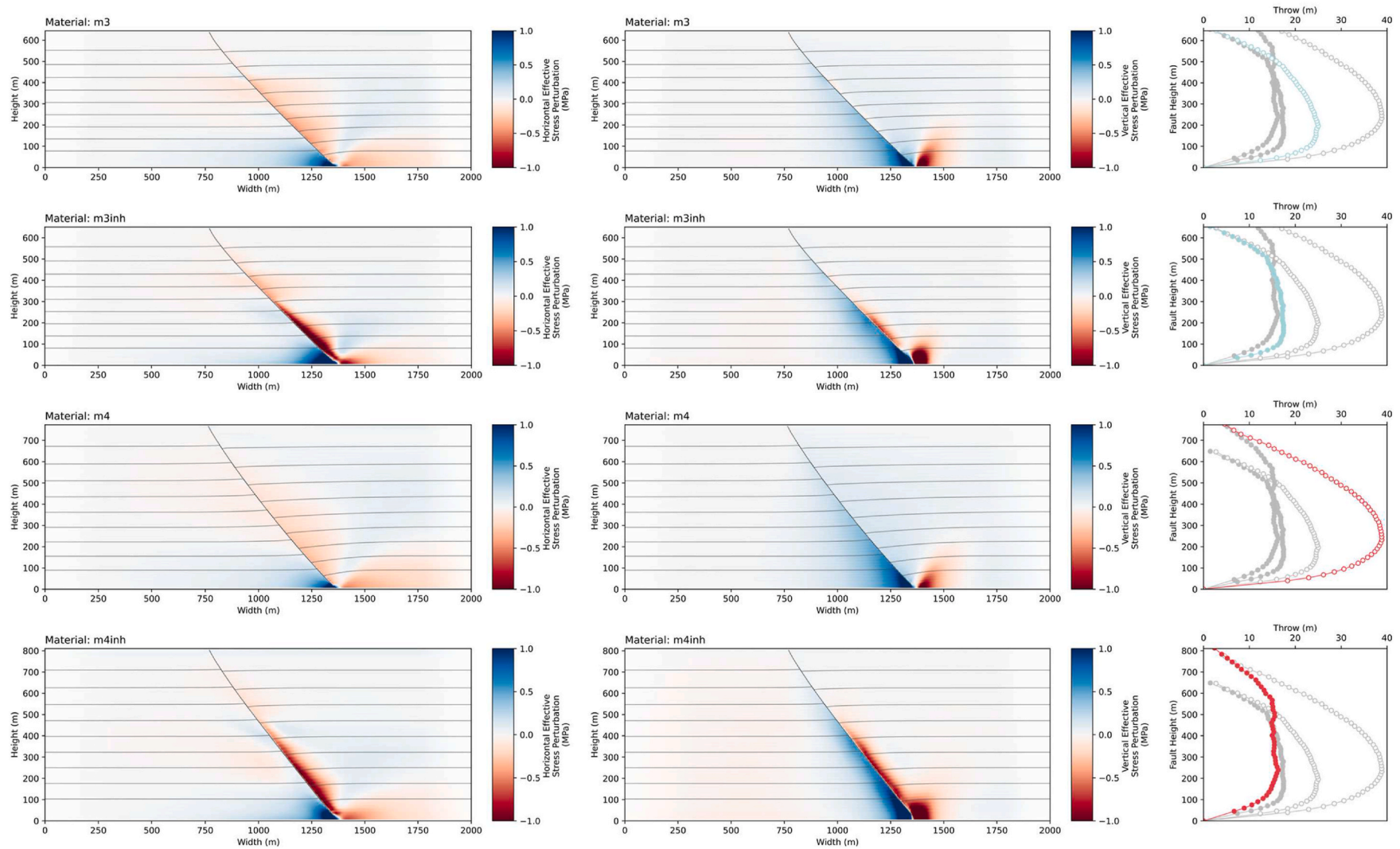


Fig. 10. Horizontal and vertical effective stress perturbation contour plots and accompanying throw versus height plots for faults with a propagating dip angle of 60° and a residual friction angle of 5° hosted in the m3, m3inh, m4, and m4inh materials at the conclusion of their respective 10 million-year simulations.

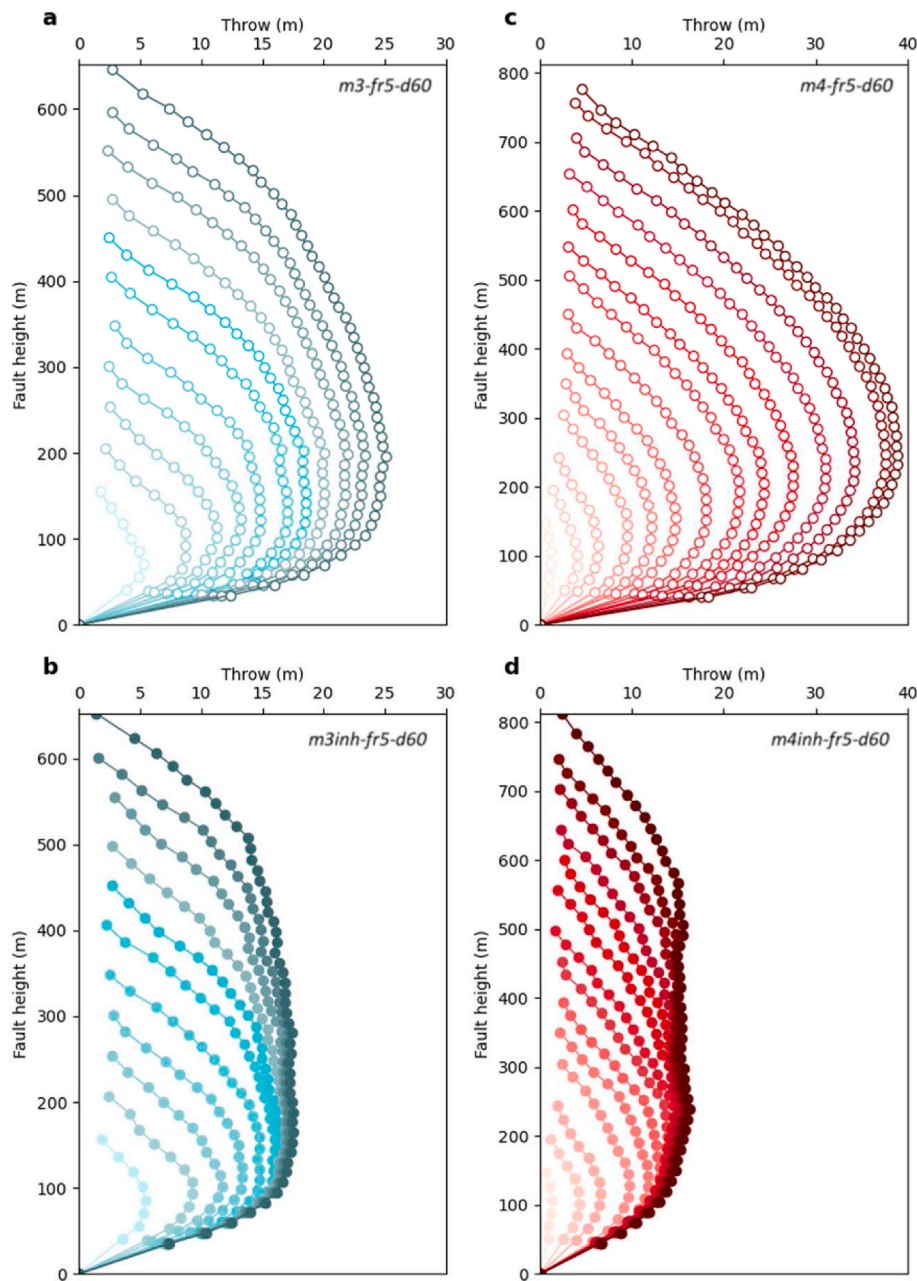


Fig. 11. The evolution of throw versus height profiles for faults with a propagating dip angle of 60° and a residual friction angle of 5° hosted within compacting and non-compacting materials: (a) m3 material, (b) m3inh material, (c) m4 material, and (d) m4inh material.

3.2. Dip angles and fault throw

To examine the impact of fault dip on fault growth, we simply selected the material and friction angle most likely to yield the maximum throw values, i.e. the m1 material with a residual friction angle of 5°. During each model simulation, the effect of increasing burial was to reduce the dip of the initial fault plane as a result of compaction of the entire cross-section. This decrease of dip due to compactional flattening has been observed for polygonal fault dips in a detailed study from offshore Norway (Neagu et al., 2010) (Figs. 5 G & 14) but is likely to occur generally (Stuevold et al., 2003; Cartwright, 2011). It is worth noting that throw is not a good proxy for displacement as the dip decreases with increasing burial depth, and this should be borne in mind when examining the plots.

For the four model simulations of varying initial dips of 40, 50, 60 and 70°, the largest throw values accumulated on faults that propagated

with an initial dip of 60° (Figs. 14–16). Interestingly, smaller throws were measured for faults with greater and lesser initial dips (Fig. 5 D & F and Fig. 15). Faults with dip propagation angles of 40°, 50°, 70°, and 80° yield T_{\max} values of 61%, 87%, 83%, and 31%, respectively, of that obtained for an initial dip of 60° (Fig. 5 F). The throw versus height plots reveal (Figs. 15 and 16) that steeply dipping fault planes yield more evenly distributed ‘C-shaped’ throw versus height profiles and shallower dipping fault planes yield ‘L-shaped’ throw versus height profiles with greater throw values skewed to the lower portions of the fault (Muraoka and Kamata, 1983; Turrini et al., 2017). At the maximum fault height achieved at the end of the m1 material simulations, the joint-steepest gradients of the T_{\max} versus fault height trends are found on the faults with propagating dip angles of 60° and 70° (Fig. 5 D). When taking account of compaction of the dip angle (Figs. 5 G & 14), the average compacted dips of the 60° and 70° cases are ~40°–50° and ~50°–60° respectively. This is consistent with the stress decomposition of an

overburden load with respect to a fracture plane, where the maximum shear stress occurs at a 45° angle to the maximum principal stress (Fossen, 2016).

3.3. Residual friction angles and fault throw

To explore the sensitivity of fault growth to variation in the residual friction angle, models were run with a fault plane with a propagation dip of 60° hosted in each of the m1-m4 materials over residual friction angles of 5°, 7°, 9°, and 11° (Table 1). For fixed values of fault dip and material properties, throw values are always highest on faults with the lowest residual friction angles (Fig. 5 C). Maximum throw values decrease exponentially with increasing residual friction angles, reaching zero when the fault plane friction angle equals the host material peak friction angle (Fig. 5 E).

At residual friction angles of 5°, all four of the material characterisations yield high maximum throw values with respect to the fault height, with values in the upper range of those recorded from polygonal fault systems (Shin et al., 2010). As the residual friction angle increases to 7°, the maximum throw values with respect to fault height derived from our four material models decrease by ~45%, with values in the mid-lower end of those recorded polygonal fault systems (Shin et al., 2010). An increase in the residual friction angle by a further two degrees to 9° yields maximum throw with respect to fault height values that are below the lowest values recorded from polygonal fault systems. At residual friction angles of 11° throw does not accumulate in measurable quantities across the fault plane. If the model results can legitimately be extrapolated to natural systems, this suggests that polygonal faults do not accumulate displacement at residual friction angles greater than 11° under fully drained gravitational loading conditions (Figs. 5 C and 17).

3.4. Throw versus height profiles

The throw versus height profiles derived from our models (Figs. 6, 9, 12, 15, 17 and 19) are comparable to those derived from PFS studies from basins around the world (Morgan et al., 2015; Turrini et al., 2017; Wrona et al., 2017). Common to all the simulated throw versus height profiles is the steeper lower tip gradient compared to the upper tip gradient (Table 2 and Fig. 19). A greater proportion of the throw accrues in the lower third and central third of the tier. Fault throw versus height profiles have curved ‘C-shaped’ or ‘L-shaped’ geometries for material models with high degrees of compaction. For the m3inh and m4inh simulations, which incorporate layers that do not compact, the throw versus height profiles have a flatter ‘M-shaped’ central portion and lower maximum throw with respect to fault height values (Table 2 and Figs. 11 and 19).

An example of the temporal evolution of throw with respect to increasing fault height is illustrated in Fig. 6. Here fault throw accumulates proportionately with successive fault propagation and sedimentation throughout the temporal evolution of our models. Throw versus height plots have quasi-symmetric profiles in the earliest phases of growth (≤ 2.5 million-years) that become more asymmetric with continued fault growth through time (≥ 5 million-years), where greater throw values are skewed towards the lower third of the fault.

3.5. Throw rates

Throw rates measured for the final million years of each model simulation range between 0 and 10.45 m/m.y. The fastest throw rates were recorded on the faults with the greatest T_{\max} values as a percentage of the fault height (Table 2 and Fig. 20). The measured throw rates increase temporally throughout the evolution of the models, reflecting the greater amounts of throw that accumulate at each subsequent timestep because of the larger thickness of differentially compacting sediment in the footwall and hanging wall as the fault height increases (Fig. 20). The throw rates recorded from our model simulations exhibit the same range

as those recorded from a PFS in the Vøring Basin, where similar sedimentation rates are recorded to those used in our models (King and Cartwright, 2020).

3.6. Stress field perturbations

The effective stress outputs from the models (Figs. 6, 7, 9, 10, 12, 13, 15–18) reveal a consistent pattern of effective mean stress perturbations in both the fault footwalls and hanging walls. The lower region of the footwalls closest to the base of each model exhibit reduced effective stress relative to the far field values and hence are ‘shadowed’ from the full extent of the overburden load. In contrast the basal regions of hanging walls exhibit enhanced effective stress values because frictional sliding on the fault plane facilitates a rotation of the principal stress axes (Fig. 8). Enhanced effective mean stress anomalies dissipate to the background values within a few hundred metres of the fault. The shapes of these anomalous regions of enhanced or reduced effective stress vary from model to model, but in general the magnitude of these stress anomalies corresponds well to the parameter combinations which yield the greatest throw values.

The horizontal effective stress perturbations are elevated in a triangular region adjacent to the fault plane and in a basal region at the lower tier boundary in the fault hanging wall. The horizontal effective stress perturbations are reduced (blue colours) in the lowermost footwall and in a dilational triangular zone in the hanging wall that separates the two aforementioned elevated areas, which is associated with the hinge of bed rotation caused by frictional sliding on the fault plane. The vertical effective stress perturbations are elevated in a circular shaped focal region at the base of the fault hanging wall, and are reduced in a ~100 m radius of the fault plane in both the footwall and hanging wall.

The effective mean stress (and both the vertical and horizontal components) perturbations are greater in the m3inh and m4inh material models which stop compacting at depths in excess of ~350 m. In the m3inh and m4inh cases, the focal regions of effective stress perturbations migrate upward across the portion of the fault plane hosted within non-compacting strata (Figs. 9 and 10). The lateral boundaries of all simulations exhibit unperturbed one-dimensional consolidation stress fields.

4. Discussion

Our study aimed to evaluate the model suggested by Goult (2001, 2002) for gravitational loading as a mechanism to explain the growth of polygonal faults. We designed a numerical modelling programme to evaluate the impact of varying the residual friction on the fault and its dip on the stress state adjacent to a single polygonal fault under protracted burial and loading conditions (Fig. 3). We attempted to capture the realistic range of compaction parameters for the typical sediments that are known to host polygonal faults and used these material models as a third variable in a set of sensitivity analyses. Our results allow us to propose some general inferences that may be directly applicable in natural fault systems.

4.1. Stress perturbations and differential compaction

A key finding of this study is that if a fault is characterised by uniformly distributed, residual friction values of 9° or less, then for a wide range of fault dips there is a measurable perturbation in the state of stress around the fault, with stress shadowing in the footwall, and localised stress enhancement in the hanging wall, particularly evident close to the basal tier boundary. These stress perturbations include components of both vertical and horizontal stress increase/decrease. This implies that simply under purely passive gravitational loading with no lateral strain (the formally defined K_0 loading condition, Lambe and Whitman, (1994)) under which polygonal faults are widely believed to form (Cartwright and Lonergan, 1996), there is a significant component

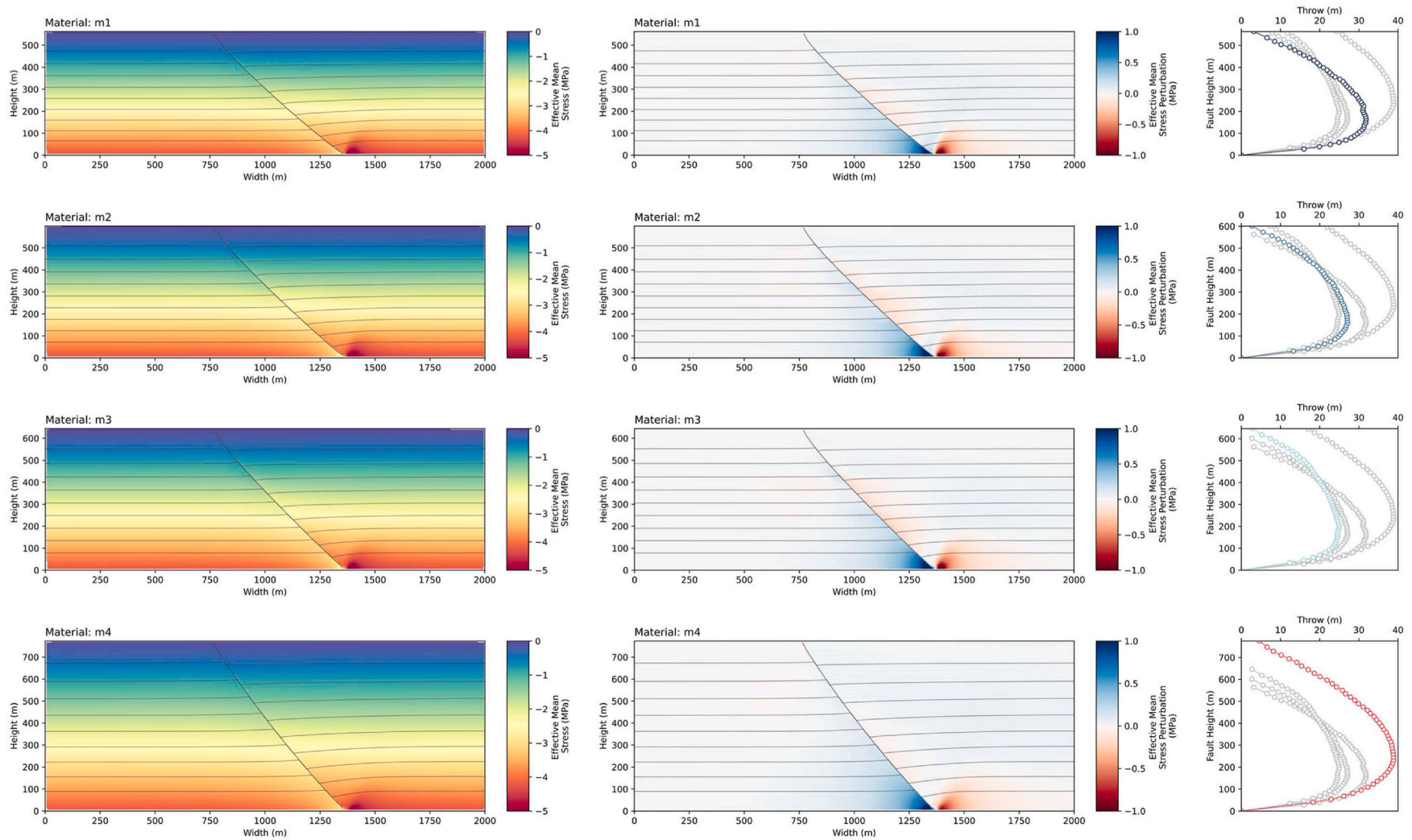


Fig. 12. Effective mean stress and perturbation contour plots and accompanying throw versus height plots for faults with a propagating dip angle of 60° and a residual friction angle of 5° hosted in the m1, m2, m3, and m4 materials at the conclusion of their respective 10 million-year simulations.

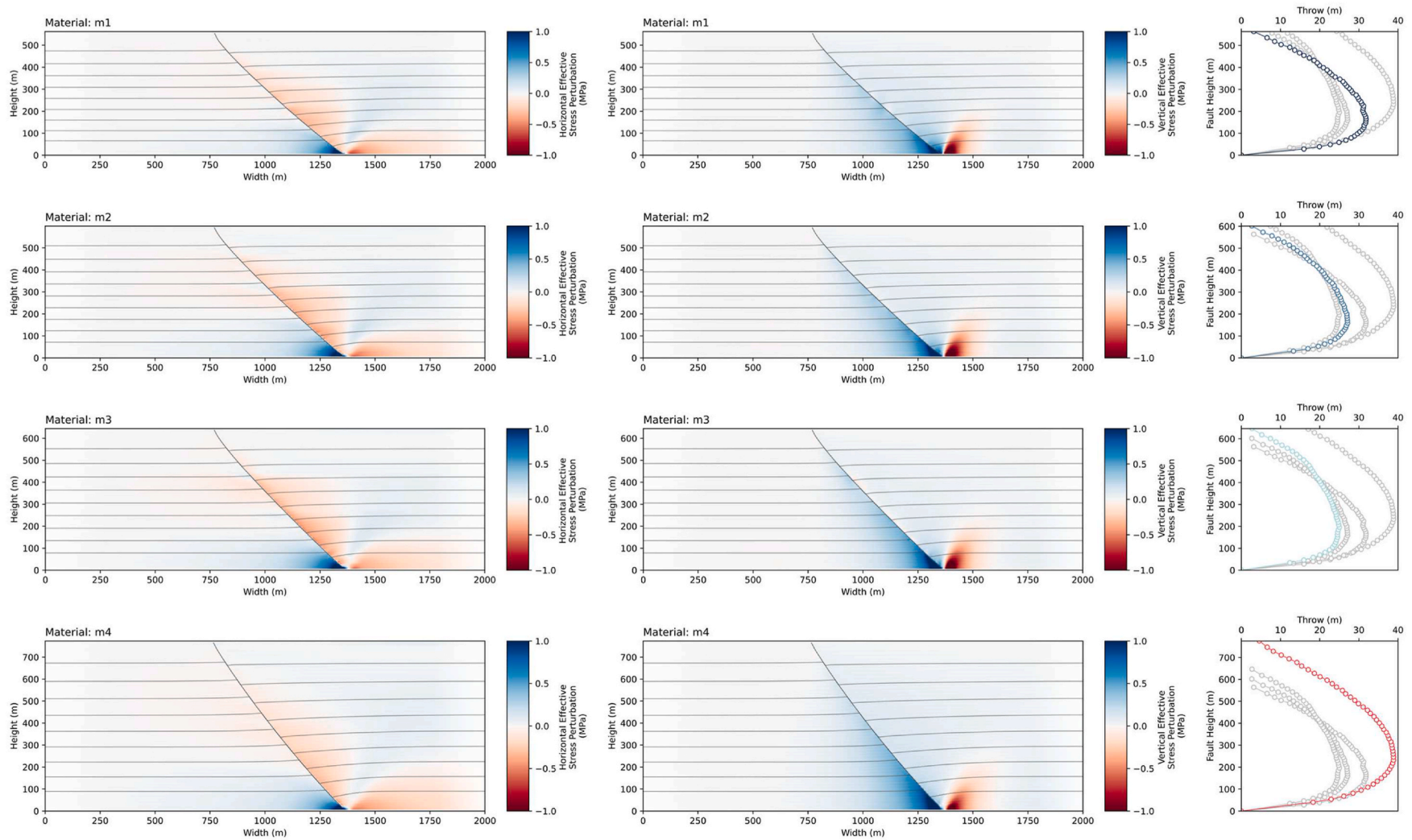


Fig. 13. Horizontal and vertical effective stress perturbation contour plots and accompanying throw versus height plots for faults with a propagating dip angle of 60° and a residual friction angle of 5° hosted in the m1, m2, m3, and m4 materials at the conclusion of their respective 10 million-year simulations.

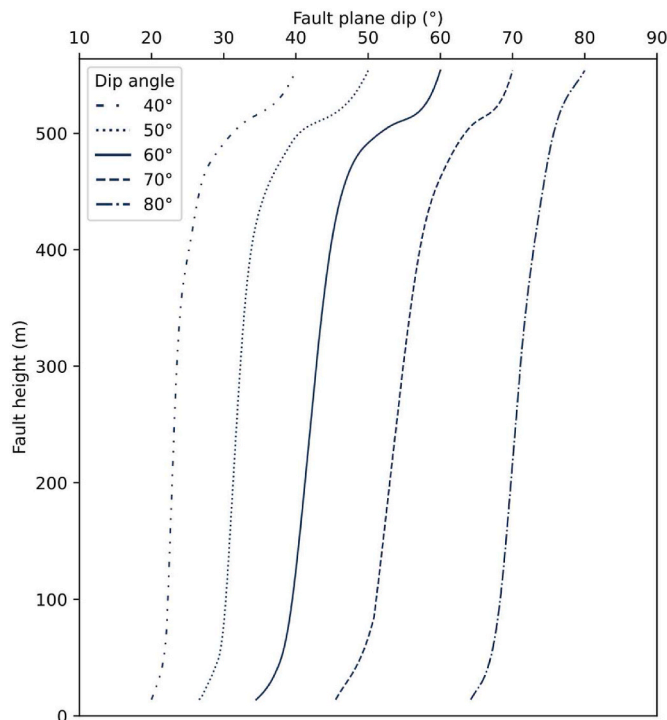


Fig. 14. Fault plane dip versus fault height for faults with different propagating dip angles hosted in the m1 material at the conclusion of the 10 million-year simulations.

of horizontal compaction and hence line length reduction in a bed-parallel direction, as argued by Goult (2002). Furthermore, the perturbation in the stress field results in a fundamental asymmetry across the fault and that in turn leads to differential volumetric strains across the fault, and it is this differential straining that necessitates semi-continuous slip on the fault surface to accommodate the wall rock strains of different magnitudes.

In soft, un lithified, fine grained sediments of the types typically found to host PFSs, it is most probable that the volumetric strain is expressed as porosity loss, but clearly other forms of strain are possible, including fracturing, stylolite formation and compaction bands (Hibsch et al., 2003; Faÿ-Gomord et al., 2017). For simplicity, we therefore consider this type of fault growth as a form of differential compaction faulting, whereby purely vertical gravitational loading is partitioned by the low friction on the fault and leads to a component of slip on such a pre-defined fault.

Differential compaction faults can develop in a range of contexts but have previously been linked to lateral changes in compaction properties such as across carbonate reefs or channel sands encased in muddy sediments, or to differential compaction on the flanks of basement highs draped by muddy sediments (Powers, 1922; Carver, 1968; Labute and Gretener, 1969; O'Connor and Gretener, 1974; Gay Jr, 1989; Laubach et al., 1999). The addition here of a mechanism to produce differential compaction faulting clearly has fundamental implications for the growth of polygonal faults, as shown by our modelling, but it extends beyond PFSs to any fault that by virtue of its low residual friction perturbs the stress state related to vertical loading under gravity.

4.2. Fault scaling relationships

One of the central arguments developed by Shin et al. (2010) in the first attempt to model polygonal fault kinematics was that extremely low bulk stiffnesses of the host medium would be required to achieve the displacement-height ratios recorded from natural systems. In contrast, our results suggest that the empirical scaling relationship between the

maximum throw values and heights of polygonal faults (Shin et al., 2010) can be replicated via simple differential compaction across pre-existing faults with uniformly distributed residual friction values less than $\sim 9^\circ$ hosted in fine-grained sediments with a range of compaction profiles (Fig. 5). Our results suggest that the accumulation of throw on polygonal faults is most sensitive to changes in the residual friction angle, and hence much of the scatter in global plots of throw versus fault height (Shin et al., 2010) may be due to variations in friction angle within a fault population. One caveat should be applied here: our model assumes an initial stage of fault nucleation and growth before gravitational loading dominates the strain accumulation, and some of the throw on any given fault should therefore be rightly ascribed to the initial stages of nucleation and propagation.

4.3. Incremental addition of displacement during fault growth

We have argued the case for syn-sedimentary growth of polygonal faults, whereby after an initial phase, the upper tip is constantly at or close to the sediment-water interface. This argument is founded in the many previous observations of PFSs in previous studies that have demonstrated growth packages, or anomalously high expansion indices or displacement gradients, or more tellingly, shown the upper tips to crop out as surface scarps (King and Cartwright, 2020, and references therein). Our model outputs consistently show that the locus of maximum throw at any increment in time migrates upwards in tandem with the general burial and addition of sediment layers to the upper boundary of the tier (Fig. 10). In short, as the tier grows vertically, the faults propagate upwards and the T_{\max} position also migrates upwards. The final position of the T_{\max} does not therefore coincide with a nucleation position in the tier as has been suggested (Watterson et al., 2000; Wrona et al., 2017; Turrini et al., 2017) but is a final snapshot of a transient, migratory process. The upward migration of the T_{\max} position with growth for polygonal faults was first suggested by Morgan et al. (2015), and this proposition is therefore confirmed by our modelling.

One other aspect of the gross kinematics of polygonal faults is that of the rate of accumulation of displacement. Until recently, this important parameter was unquantified for polygonal faults, but King and Cartwright (2020) were able to correlate markers from Ocean Drilling Project cores and from these measure displacement rates of the order of 1–10 m/m.y. The throw rates derived from our models are consistent with those recorded from the upper tips of their surface-breaching polygonal faults in the Vøring Basin. It is worth noting that those faults are hosted in a tier with similar sedimentation rates to those used in our models, and it is tempting to speculate that displacement rates for faults undergoing some form of fault-perturbed differential compaction would most likely scale with sedimentation (loading) rates.

4.4. Limitations with the modelling

Our modelling strategy did not attempt to replicate the three-dimensional complexity of intersecting polygonal fault geometries (Lonergan et al., 1998a) or heterogeneities between units that comprise a PFS tier (Cartwright et al., 2003; Verschuren, 2019). We characterised our models with a single continuous fault plane with a uniform residual friction angle over its entire surface. However, outcrop observations of polygonal faults show that the fault zones may comprise a multitude of smaller fractures and splays (Verschuren, 1990; Hibsch et al., 2003; Tewksbury et al., 2014; Faÿ-Gomord et al., 2017; Verschuren, 2019) that would aggregate to give the appearance of a single plane at the resolution limits of seismic reflection data. These heterogeneities and fault intersections may explain the differences between the smoothly tapering throw profiles produced in our simulations (Fig. 19) and the jagged or stepped throw profiles recorded from polygonal faults imaged in seismic reflection data (Neagu et al., 2010; Morgan et al., 2015; Turrini et al., 2017; Wrona et al., 2017). However, despite the relative homogeneity of our models compared to real PFS tiers, our results successfully reproduce

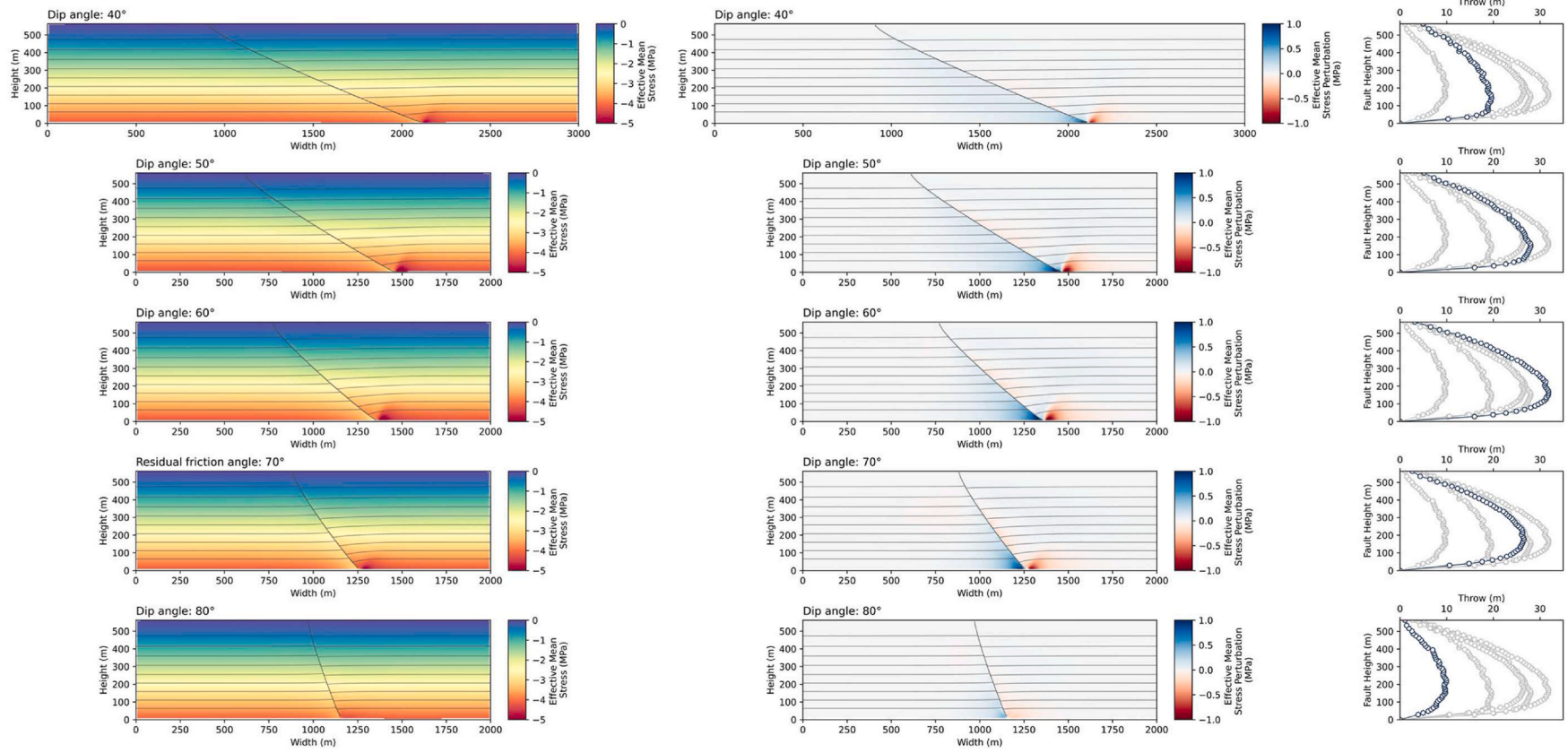


Fig. 15. Effective mean stress and perturbation contour plots and accompanying throw versus height plots for faults hosted in the m1 material and a residual friction angle of 5° with propagating dip angles of 40°, 50°, 60°, 70°, and 80° at the conclusion of their respective 10 million-year simulations.

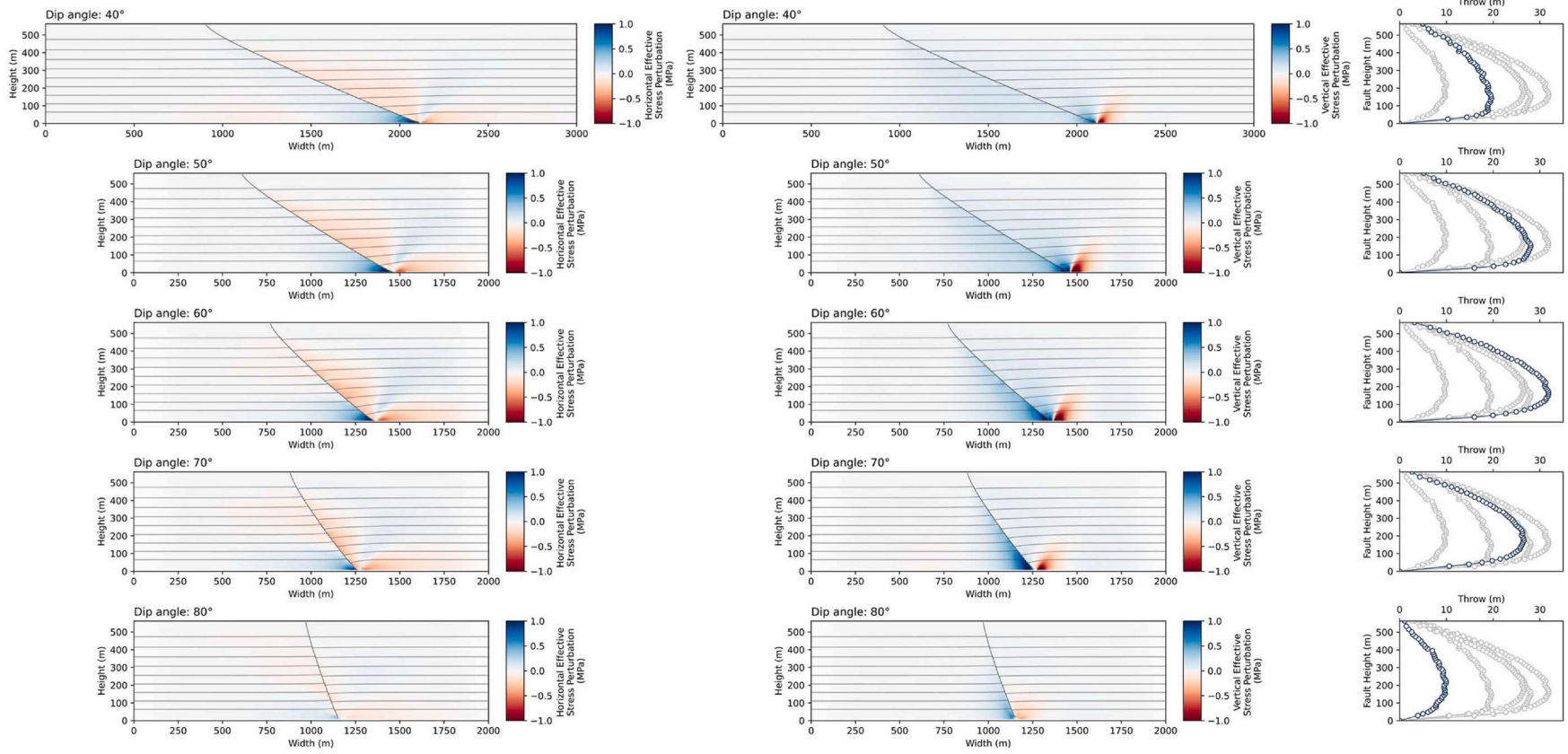


Fig. 16. Horizontal and vertical effective stress perturbation contour plots and accompanying throw-versus-height plots for faults hosted in the m1 material and a residual friction angle of 5° with starting dip angles of 40°, 50°, 60°, 70°, and 80° at the conclusion of their respective 10 million-year simulations.

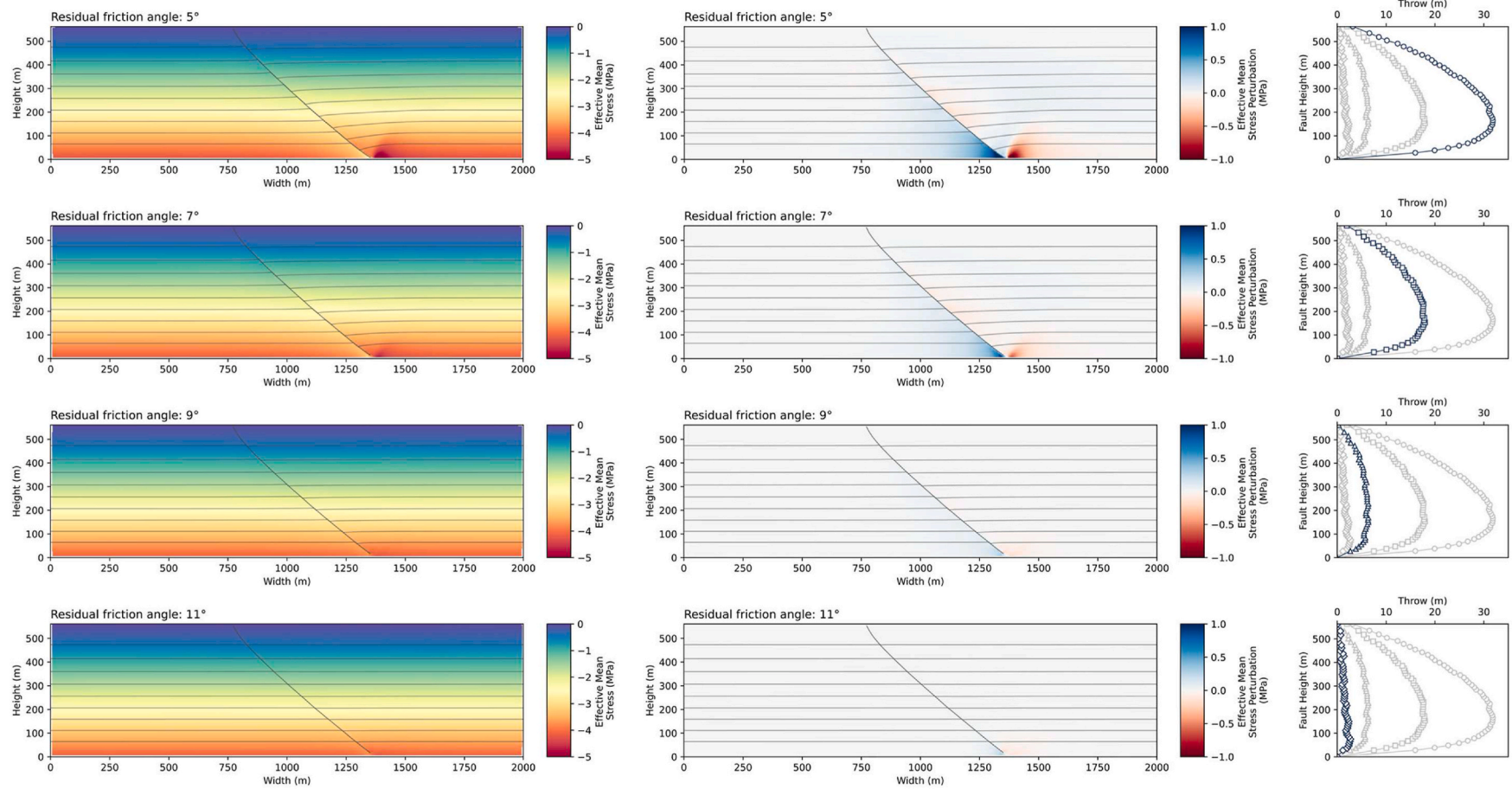


Fig. 17. Effective mean stress and perturbation contour plots and accompanying throw versus height plots for faults hosted in the m1 material with a propagating dip angle of 60° and residual friction angles of 5° , 7° , 9° , and 11° at the conclusion of their respective 10 million-year simulations.

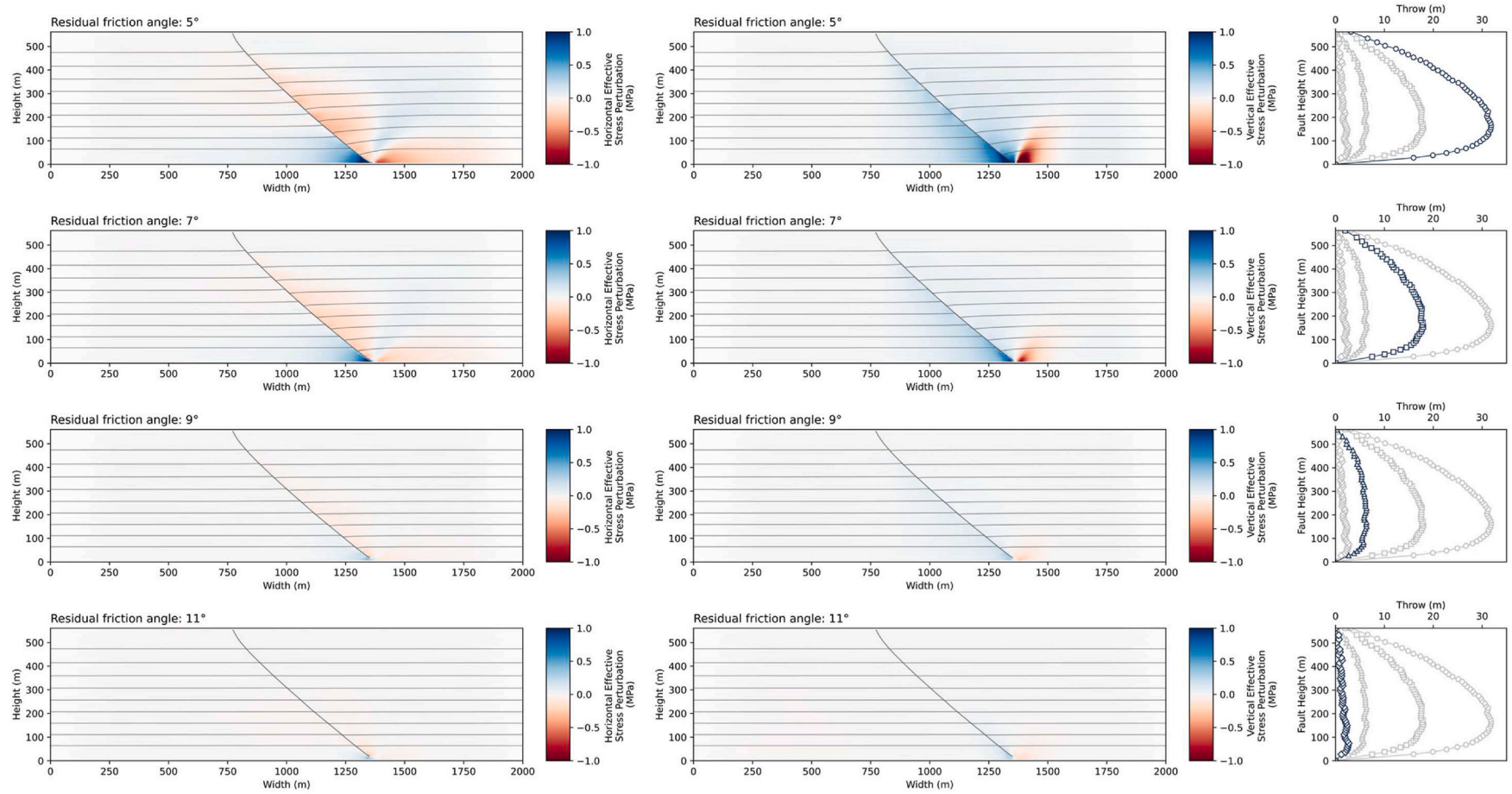


Fig. 18. Horizontal and vertical effective stress perturbation contour plots and accompanying throw versus height plots for faults hosted in the m1 material with a propagating dip angle of 60° and residual friction angles of 5°, 7°, 9°, and 11° at the conclusion of their respective 10 million-year simulations.

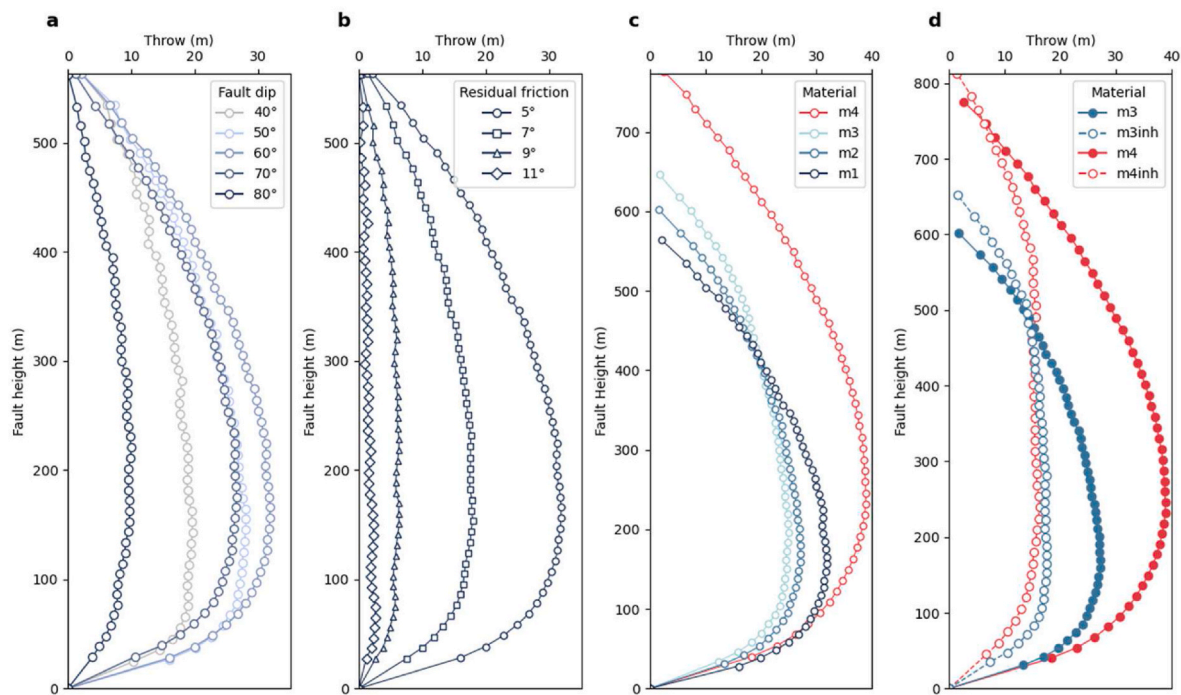


Fig. 19. Throw versus fault height profiles for faults at the end of the 10 million-year simulation: (a) with propagating dip angles between 40° and 80°, hosted in the m1 material with a residual friction angle of 5°; (b) with residual friction angles between 5° and 11°, hosted in the m1 material with a propagating dip angle of 60°; (c) hosted in the m1, m2, m3, and m4 materials, with a residual friction angle of 5° and an initial fault dip angle of 60°; (d) hosted in the m3, m3inh, m4, and m4inh materials, with a residual friction angle of 5° and a propagating dip angle of 60°.

Table 2

Upper and lower tip gradients, maximum throw values, and throw rates for faults with different material compaction profiles, propagating dip angles, and residual friction angles from our sensitivity analysis. All values are measured at the conclusion of each respective simulation at the 10 million-year timestep.

Model simulation	Upper tip gradient	Lower tip gradient	Maximum throw (m)	Fault height (m)	Maximum throw/Fault height	Throw rate (m/m.y.)
m1-fr5-d60	0.108	0.480	31.84	564	5.65%	10.45
m1-fr7-d60	0.063	0.258	17.96	564	3.18%	6.54
m1-fr9-d60	0.028	0.099	6.38	564	1.13%	3.25
m1-fr5-d40	0.055	0.362	19.64	564	3.48%	5.38
m1-fr5-d50	0.084	0.477	28.02	564	4.97%	7.56
m1-fr5-d70	0.093	0.357	26.59	564	4.71%	8.48
m1-fr5-d80	0.032	0.128	9.94	564	1.76%	2.33
m2-fr5-d60	0.098	0.378	27.12	602	4.50%	9.58
m3-fr5-d60	0.091	0.322	25.04	647	3.87%	9.09
m4-fr5-d60	0.096	0.398	38.86	776	5.00%	9.63
m3inh-fr5-d60	0.092	0.212	17.48	653	2.68%	4.63
m4inh-fr5-d60	0.060	0.139	16.29	813	2.00%	4.18

the ‘C-, M-, and L-shaped’ geometries of polygonal fault throw profiles.

One of the main limitations of this study was that we did not explicitly investigate the role of overpressure. Elevated fluid pressure may facilitate the episodic growth of some polygonal faults at higher residual friction angles, and contribute to the growth of polygonal faults that span ultra-low permeability fine-grained units which may experience periods of compaction disequilibrium. If, for example, a polygonal fault ceases its growth because of an increase in the fault friction angle, then fluid pressure may build with increasing burial depth in undrained units until the fluid pressure acting on the fault plane reduces the effective mean stress sufficiently to facilitate frictional sliding at low shear stresses (Bolton et al., 1998; Watterson et al., 2000), thus reactivating fault growth. It is worth noting that overpressured mobile units found at the base of fine-grained sedimentary tiers may act as décollement surfaces and these overpressured unit have been suggested as a means to nucleate PFS (Watterson et al., 2000). However, investigating the nucleation of PFS was beyond the scope of this study, which focused solely on the drivers of post-nucleation growth.

4.5. Wider implications of the modelling results

The arrest and termination of activity on the constituent faults (‘death’) making up a PFS may occur once the host sedimentary units no longer undergo differential volumetric strain. This may occur from the base of the tier upwards in a burial conveyor-belt like fashion, or in a single fossilisation phase. The slowing and ultimate cessation of differential volumetric strain may occur as frictional sliding is inhibited by an increase in the residual friction angle and/or the slowing of volumetric change of the host units caused by lithification. The upward termination of a PFS may also occur because of a depositional facies change (Cartwright et al., 2003; Jackson et al., 2014), and the growth of individual polygonal faults within a PFS may be inhibited by the intersection of neighbouring faults (Lonergan et al., 1998a). Fluctuations in the overburden loading rate (both erosional and depositional) may also influence the growth of PFSs. Faster sedimentation rates may increase the rate of compaction in drained conditions or drive overpressure in undrained conditions, therefore driving faster throw rates but also greater PFS tier heights (c.f. the empirical scaling relationship established by

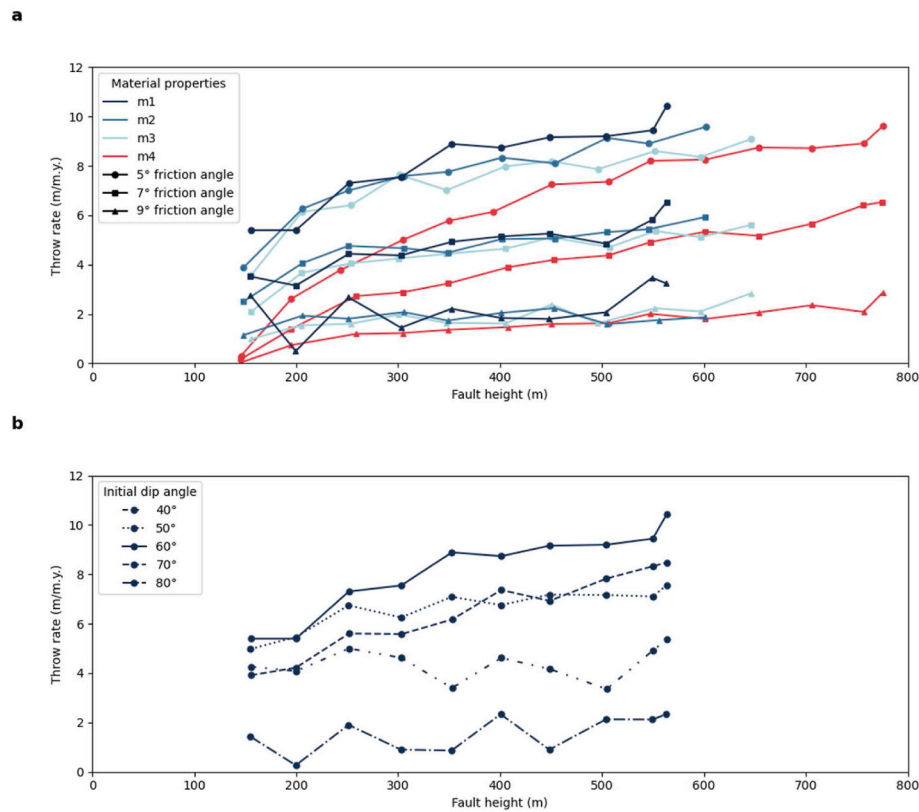


Fig. 20. Throw rate with respect to fault height measured as the amount of throw accumulated on the stratigraphic marker deposited 1 million-years earlier for: (a) materials m1, m2, m3, and m4 over residual friction angles of 5°, 7°, and 9° on a fault plane with a propagating dip angle of 60°; (b) faults with propagating dip angles of 40°, 50°, 60°, 70°, and 80° hosted in the m1 material with a residual friction angle of 5°.

Shin et al. (2010)). Erosional events or depositional hiatuses may, on the other hand, limit the subsequent accrual of differential compaction until the pre-erosional maximum effective stress is reached following re-loading, in which time the material physical properties may have changed to inhibit further differential compaction. In summary, the temporal evolution of individual polygonal faults within a tier may be governed by many factors. However, our sensitivity analysis suggests that the growth of polygonal faults is primarily driven by low residual friction angles on dipping fault planes which facilitate differential compaction.

In summary, the results presented in this study strongly suggest that the growth of normal faults hosted in laterally-pinned sedimentary tiers can be solely facilitated by gravity-driven differential compaction at low residual friction angles. A gravity-driven differential compaction mechanism is likely the overarching driver of the growth of polygonal fault systems universally, where processes such as overpressure and diagenetically-induced volumetric reductions may act as secondary and tertiary contributing factors, respectively, to enhance or reactivate polygonal faults in some circumstances. In addition to the growth of PFSS, a differential compaction mechanism may also explain why up-dip extensional strains are consistently greater than down-dip compressional strains recorded in shallowly buried gravitational-slope fault systems found on continental shelves (Dalton et al., 2015).

5. Conclusions

In this study, we modelled the growth of an isolated fault hosted within laterally-pinned conditions with respect to variable material compaction profiles, residual friction angles, and fault dip angles, using a suite of two-dimensional finite element forward models constructed in ELFE, that coupled upward fault propagation with simultaneous sedimentation and compaction of unconsolidated fine-grained granular

sediment. Our results show for the first time, that faults hosted in laterally-pinned conditions – such as those that host polygonal fault systems – can accumulate throw solely through gravity-driven differential compaction under realistic physical property and burial conditions.

The main findings of this study are:

- (1) Polygonal fault systems grow as the result of gravity-driven differential compaction at low residual friction angles.
- (2) Maximum throw (T_{max}) as a percentage of fault height values recorded from polygonal fault systems globally (~6%) can be achieved at standard fault dip angles and material property values typical of those recorded from fine-grained sediments at residual friction angles <9°.
- (3) Throw rates derived from our sensitivity analysis (0–10.45 m/m.y.) are consistent with recently recorded ultra-slow throw rates from the upper tips of polygonal faults in the Vøring Basin, Norwegian Sea (1.4–10.9 m/m.y.).

Author statement

James J. King: Conceptualisation, Methodology, Investigation, Writing – Original Draft, Visualisation.

Daniel T. Roberts: Supervision, Methodology, Software, Validation.

Joe A. Cartwright: Supervision, Conceptualisation, Writing – Review & Editing.

Bruce K. Levell: Supervision, Writing – Review & Editing.

Declaration of competing interest

The authors declare that they have no known competing financial interests or personal relationships that could have appeared to influence

the work reported in this paper.

Acknowledgements

The UK Natural Environment Research Council (NE/M00578X/1) and the Oxford-Radcliffe Scholarship are thanked for funding J. King's DPhil research. We thank Rockfield Global for providing an ELFEN finite element modelling software license. We thank Prof J. Walsh for his insightful review of this work in J. King's DPhil examination, which greatly improved the quality of the manuscript. M. Foschi and C. Kirkham are thanked for many helpful discussions.

Appendix A. Supplementary data

Supplementary data to this article can be found online at <https://doi.org/10.1016/j.jsg.2022.104679>.

Alternative Draft Highlights.

- Differential compaction drives growth of laterally-pinned polygonal fault systems

References

- Albertz, M., Lingrey, S., 2012. Critical state finite element models of contractional fault-related folding: Part 1. Structural analysis. In: *Tectonophysics* 576, pp. 133–149.
- Armandita, C., Morley, C.K., Rowell, P., 2015. Origin, structural geometry, and development of a giant coherent slide: the South Makassar Strait mass transport complex. *Geosphere* 11.2, 376–403.
- Berndt, C., Büinz, S., Mienert, J., 2003. Polygonal fault systems on the mid-Norwegian margin: a long-term source for fluid flow. *Geol. Soc. Lond. Spec. Publ.* 216, 283–290, 1.
- Berndt, C., Jacobs, C., Evans, A., Gay, A., Elliott, G., Long, D., Hitchen, K., 2012. Kilometre-scale polygonal seabed depressions in the Hatton Basin, NE Atlantic Ocean: constraints on the origin of polygonal faulting. In: *Marine Geology* 332, pp. 126–133.
- Bishop, A.W., Green, G., Garga, V.K., Andresen, A., Brown, J., 1971. A new ring shear apparatus and its application to the measurement of residual strength. *Geotechnique* 21 (4), 273–328.
- Bolton, A., Maltman, A., Clennell, M., 1998. The importance of overpressure timing and permeability evolution in fine-grained sediments undergoing shear. *J. Struct. Geol.* 20 (8), 1013–1022.
- Cartwright, J.A., 1994a. Episodic basin-wide fluid expulsion from geopressed shale sequences in the North Sea basin. *Geology* 22 (5), 447–450.
- Cartwright, J.A., 1994b. Episodic basin-wide hydrofracturing of overpressured early cenozoic mudrock sequences in the north sea basin. *Mar. Petrol. Geol.* 11 (5), 587–607.
- Cartwright, J.A., 2011. Diagenetically induced shear failure of fine-grained sediments and the development of polygonal fault systems. *Mar. Petrol. Geol.* 28 (9), 1593–1610.
- Cartwright, J.A., Dewhurst, D.N., 1998. Layer-bound compaction faults in fine-grained sediments. *Geol. Soc. Am. Bull.* 110 (10), 1242–1257.
- Cartwright, J.A., James, D., Bolton, A., 2003. The Genesis of Polygonal Fault Systems: a Review. *Geol. Soc. Lond. Spec. Publ.* 216, 223–243, 1.
- Cartwright, J.A., Lonergan, L., 1996. Volumetric contraction during the compaction of mudrocks: a mechanism for the development of regional-scale polygonal fault systems. *Basin Res.* 8 (2), 183–193.
- Carver, R.E., 1968. Differential compaction as a cause of regional contemporaneous faults. *AAPG (Am. Assoc. Pet. Geol.) Bull.* 52 (3), 414–419.
- Casey, B.B.A., 2014. The Consolidation and Strength Behavior of Mechanically Compressed Fine-Grained Sediments. PhD thesis. Massachusetts Institute of Technology.
- Cripps, J., Taylor, R., 1981. The engineering properties of mudrocks. *Q. J. Eng. Geol. Hydrogeol.* 14 (4), 325–346.
- Crook, A.J.L., Willson, S., Yu, J., Owen, D., 2006. Predictive modelling of structure evolution in sandbox experiments. *J. Struct. Geol.* 28 (5), 729–744.
- Dalton, T.J.S., Paton, D.A., Needham, T., Hodgson, N., 2015. Temporal and spatial evolution of deepwater fold thrust belts: implications for quantifying strain imbalance. In: *Interpretation* 3.4, SAA59–SAA70.
- Davies, R.J., Ireland, M.T., 2011. Initiation and propagation of polygonal fault arrays by thermally triggered volume reduction reactions in siliceous sediment. *Mar. Geol.* 289 (1–4), 150–158.
- Dewoolkar, M.M., Huzjak, R.J., 2005. Drained residual shear strength of some claystones from Front Range, Colorado. *J. Geotech. Geoenviron. Eng.* 131 (12), 1543–1551.
- Fay-Gomord, O., Allan, C., Verbiest, M., Lasseur, E., Swennen, R., Gauthier, B., 2017. Synsedimentary polygonal faults system in tight chalk: multiscale evidence from outcrop, flamborough head (UK). In: 79th EAGE Conference and Exhibition 2017, vol. 2017. European Association of Geoscientists & Engineers, pp. 1–5, 1.
- Finch, E., Hardy, S., Gawthorpe, R., 2003. Discrete element modelling of contractional fault-propagation folding above rigid basement fault blocks. *J. Struct. Geol.* 25 (4), 515–528.
- Fossen, H., 2016. *Structural Geology*. Cambridge University Press.
- Gay, A., Berndt, C., 2007. Cessation/reactivation of polygonal faulting and effects on fluid flow in the Vøring Basin, Norwegian Margin. *J. Geol. Soc.* 164 (1), 129–141.
- Gay Jr., S.P., 1989. Gravitational compaction, a neglected mechanism in structural and stratigraphic studies: new evidence from Mid-Continent, USA. *AAPG Bull.* 73 (5), 641–657.
- Goult, N.R., 2001a. Mechanics of layer-bound polygonal faulting in fine-grained sediments. *J. Geol. Soc.* 159 (3), 239–246.
- Goult, N.R., 2001b. Polygonal fault networks in fine-grained sediments – an alternative to the syneresis mechanism. *First Break* 19 (2), 69–73.
- Goult, N.R., 2008. Geomechanics of polygonal fault systems: a review. *Petrol. Geosci.* 14 (4), 389–397.
- Goult, N.R., Swarbrick, R.E., 2005. Development of polygonal fault systems: a test of hypotheses. *J. Geol. Soc.* 162 (4), 587–590.
- Gradmann, S., Beaumont, C., Albertz, M., 2009. Factors controlling the evolution of the Perdido Fold Belt, northwestern Gulf of Mexico, determined from numerical models. *Tectonics* 28 (2).
- Gray, G.G., Morgan, J.K., Sanz, P.F., 2014. Overview of continuum and particle dynamics methods for mechanical modeling of contractional geologic structures. *J. Struct. Geol.* 59, 19–36.
- Henriet, J., De Batist, M., Van Vaerenbergh, W., Verschuren, M., 1988. Seismic facies and clay tectonic features of the Ypresian clay in the southern North Sea. *Bull. Belg. Ver. Geol.* 97, 457–472.
- Hibsch, C., Cartwright, J., Hansen, D.M., Gaviglio, P., André, G., Cushing, M., Bracq, P., Juignet, P., Benoit, P., Allou, J., 2003. Normal faulting in chalk: tectonic stresses vs. compaction-related polygonal faulting. *Geol. Soc. Lond. Spec. Publ.* 216 (1), 291–308.
- Higgs, W., McClay, K., 1993. Analogue sandbox modelling of miocene extensional faulting in the outer moray firth. *Geol. Soc. Lond. Spec. Publ.* 71 (1), 141–162.
- Ikari, M.J., Kopf, A.J., Hüpers, A., Vogt, C., 2018. Lithologic control of frictional strength variations in subduction zone sediment inputs. *Geosphere* 14.2, 604–625.
- Jackson, C.A.-L., Carruthers, D.T., Mahlo, S.N., Briggs, O., 2014. Can polygonal faults help locate deep-water reservoirs? *AAPG (Am. Assoc. Pet. Geol.) Bull.* 98 (9), 1717–1738.
- Jones, M., 1994. Mechanical principles of sediment deformation. In: *The Geological Deformation of Sediments*. Springer, pp. 37–71.
- King, J.J., Cartwright, J.A., 2020. Ultra-slow throw rates of polygonal fault systems. *Geology* 48 (5), 473–477.
- Kopf, A., Clennell, B., Flecker, R., 1998. 49. Relationship between the variation of undrained shear strength, organic carbon content, and the origin and frequency of enigmatic normal faults in fine-grained sediments from advanced piston cores from the eastern Mediterranean. In: *Proceedings of the Ocean Drilling Program, Scientific Results*, vol. 160. Ocean Drilling Program, pp. 645–661.
- Labute, G., Gretener, P., 1969. Differential compactions around a leded reef - wizard lake area, Alberta. *Bull. Can. Petrol. Geol.* 17 (3), 304–325.
- La Gatta, D.P., 1970. Residual Strength of Clay and Clay-Shales by Rotation Shear Tests. Tech. Rep. Harvard University Soil Mechanics Lab.
- Laubach, S.E., Schultz-Ela, D.D., Tyler, R., 1999. Differential Compaction of Interbedded Sandstone and Coal. *Geol. Soc. Lond. Spec. Publ.* 169 (1), 51–60.
- Laurent, D., Gay, A., Baudon, C., Berndt, C., Soliva, R., Planke, S., Mourgues, R., Lacaze, S., Pauget, F., Mangue, M., et al., 2012. High-resolution architecture of a polygonal fault interval inferred from geomodel applied to 3D seismic data from the Gjallar Ridge, Vøring Basin, Offshore Norway. In: *Marine Geology* 332, pp. 134–151.
- Lonergan, L., Cartwright, J.A., Jolly, R., 1998a. The geometry of polygonal fault systems in Tertiary mudrocks of the North Sea. *J. Struct. Geol.* 20 (5), 529–548.
- Lonergan, L., Cartwright, J.A., Laver, R., Staffurth, J., 1998b. Polygonal faulting in the Tertiary of the central North Sea: implications for reservoir geology. *Geol. Soc. Lond. Spec. Publ.* 191–207, 127.1.
- Mandl, G., 1988. *Mechanics of Tectonic Faulting*. Elsevier.
- Mondol, N.H., Bjørlykke, K., Jahren, J., Hoeg, K., 2007. Experimental mechanical compaction of clay mineral aggregates – changes in physical properties of mudstones during burial. *Mar. Petrol. Geol.* 24 (5), 289–311.
- Moore, D.E., Lockner, D.A., 2007. Friction of the smectite clay montmorillonite. In: *The Seismogenic Zone of Subduction Thrust Faults*, pp. 317–345.
- Morgan, D.A., Cartwright, J.A., Imbert, P., 2015. Perturbation of polygonal fault propagation by buried pockmarks and the implications for the development of polygonal fault systems. *Mar. Petrol. Geol.* 65, 157–171.
- Muir Wood, D., 1990. *Soil Behaviour and Critical State Soil Mechanics*. Cambridge University Press.
- Muraoka, H., Kamata, H., 1983. Displacement distribution along minor fault traces. *J. Struct. Geol.* 5 (5), 483–495.
- Namiki, Y., Tsutsumi, A., Ujii, K., Kameda, J., 2014. Frictional properties of sediments entering the Costa Rica subduction zone offshore the Osa Peninsula: implications for fault slip in shallow subduction zones. *Earth Planets Space* 66 (1), 1–8.
- Neagu, R.C., Cartwright, J.A., Davies, R.J., 2010. Measurement of diagenetic compaction strain from quantitative analysis of fault plane dip. *J. Struct. Geol.* 32 (5), 641–655.
- Nelson, J.L., 1992. Clay mineralogy and residual shear strength of the Santa Clara formation claystone, Saratoga Foothills, California. *Bull. Assoc. Eng. Geol.* 29 (3), 299–310.
- Nicol, A., Walsh, J.J., Watterson, J., Nell, P.A.R., Bretan, P., 2003. The geometry, growth and linkage of faults within a polygonal fault system from South Australia. *Geol. Soc. Lond. Spec. Publ.* 216 (1), 245–261.

- Nikolinakou, M.A., Flemings, P.B., Hudec, M.R., 2014a. Modeling stress evolution around a rising salt diapir. *Mar. Petrol. Geol.* 51, 230–238.
- Nikolinakou, M.A., Hudec, M.R., Flemings, P.B., 2014b. Comparison of evolutionary and static modeling of stresses around a salt diapir. *Mar. Petrol. Geol.* 57, 537–545.
- O'Connor, M., Gretener, P., 1974. Quantitative modelling of the processes of differential compaction. *Bull. Can. Petrol. Geol.* 22 (3), 241–268.
- Peric, D., Crook, A.J.L., 2004. Computational strategies for predictive geology with reference to salt tectonics. *Comput. Methods Appl. Mech. Eng.* 193 (48–51), 5195–5222.
- Powers, S., 1922. Reflected buried hills and their importance in petroleum geology. *Econ. Geol.* 17 (4), 233–259.
- Roberts, D.T., Crook, A.J.L., Cartwright, J.A., Profit, M.L., Rance, J.M., et al., 2014. The evolution of polygonal fault systems: insights from geomechanical forward modeling. In: 48th US Rock Mechanics/Geomechanics Symposium. American Rock Mechanics Association.
- Rudnicki, J.W., Rice, J.R., 1975. Conditions for the localization of deformation in pressure-sensitive dilatant materials. *J. Mech. Phys. Solid.* 23 (6), 371–394.
- Roberts, D.T., 2014. A Geomechanical Analysis of the Formation and Evolution of Polygonal Fault Systems. PhD thesis. Cardiff University.
- Rockfield, 2010. *ELFEN Forward Modelling User Manual*.
- Sanada, H., Niunoya, S., Matsui, H., Fujii, Y., 2009. Influences of sedimentary history on the mechanical properties and microscopic structure change of Horonobe siliceous rocks. *J. Min. Mater. Process. Inst. Jpn.* 125 (1011), 521–529.
- Santamarina, J.C., Klein, K., Fam, M., 2001. Soils and waves: particulate materials behaviour, characterisation and process monitoring. *J. Soils Sediments* 1 (2), 196.
- Schofield, A., Wroth, P., 1968. *Critical State Soil Mechanics*. McGraw-hill.
- Schöpfer, M.P., Abe, S., Childs, C., Walsh, J.J., 2009. The impact of porosity and crack density on the elasticity, strength and friction of cohesive granular materials: insights from DEM modelling. *Int. J. Rock Mech. Min. Sci.* 46 (2), 250–261.
- Schultz-Ela, D.D., 2003. Origin of drag folds bordering salt diapirs. *AAPG Bull.* 87 (5), 757–780.
- Shin, H., Santamarina, J.C., Cartwright, J.A., 2008. Contraction-driven shear failure in compacting uncemented sediments. *Geology* 36 (12), 931–934.
- Shin, H., Santamarina, J.C., Cartwright, J.A., 2010. Displacement field in contraction-driven faults. *J. Geophys. Res. Solid Earth* 115, B7.
- Shipboard Scientific Party, 1987. Site 644: Norwegian sea. In: Eldholm, O., Thiede, J., Taylor, E., et al. (Eds.), *Proceedings of the Ocean Drilling Program, Initial Reports*, pp. 751–771.
- Shipboard Scientific Party, 1990. Site 762: exmouth Plateau. In: Haq, B.U., von Rad, U., O'Connell, S., et al. (Eds.), *Proceedings of Ocean Drilling Program, Initial Reports*, pp. 213–288, 1990122.
- Shipboard Scientific Party, 1996. Site 982: Rockall Trough. In: Jansen, E., Raymo, M.E., Blum, P., et al. (Eds.), *Proceedings of Ocean Drilling Program, Initial Reports*, pp. 91–138, 1996122.
- Shipboard Scientific Party, 2001. Site 1173: nankai Trough. In: Moore, G.F., Taira, A., Klaus, A., et al. (Eds.), *Proceedings of Ocean Drilling Program, Initial Reports*, pp. 1–147, 2001190.
- Stuevold, L.M., Faereth, R.B., Arnesen, L., Cartwright, J.A., Möller, N., 2003. Polygonal faults in the Ormen Lange field, Møre Basin, offshore mid Norway. *Geol. Soc. Lond. Spec. Publ.* 216, 263–281, 1.
- Terzaghi, K., Peck, R.B., 1948. *Soil Mechanics in Engineering Practice*. Chapman and Hall, London.
- Tewksbury, B.J., Hogan, J.P., Kattenhorn, S.A., Mehrtens, C.J., Tarabees, E.A., 2014. Polygonal faults in chalk: insights from extensive exposures of the Khoman formation, western desert, Egypt. *Geology* 42 (6), 479–482.
- Turrini, L., Jackson, C.A.-L., Thompson, P., 2017. Seal rock deformation by polygonal faulting, offshore Uruguay. *Mar. Petrol. Geol.* 86, 892–907.
- Verschuren, M., 2019. Outcrop evidence of polygonal faulting in Ypresian marine clays (Southern North Sea Basin) leads to a new synthesis. *Mar. Geol.* 413, 85–98.
- Wan, Y., Kwong, J., 2002. Shear strength of soils containing amorphous clay-size materials in a slow-moving landslide. *Eng. Geol.* 65 (4), 293–303.
- Watterson, J., Walsh, J.J., Nicol, A., Nell, P., Bretan, P., 2000. Geometry and origin of a polygonal fault system. *J. Geol. Soc.* 157 (1), 151–162.
- Wrona, T., Magee, C., Jackson, C.A.-L., Huuse, M., Taylor, K.G., 2017. Kinematics of polygonal fault systems: observations from the northern North Sea. *Front. Earth Sci.* 5, 101.